LUDWIG-MAXIMILIANS UNIVERSITÄT MÜNCHEN

MASTER THESIS

Studies on the Tile-Calorimeter Timing Measurement for a Search for heavy charged long-lived Particles in ATLAS Run–2 Data

---

Author:
Joschua KRINK

Supervisor:
Dr. habil. Sascha MEHLHASE

A thesis submitted in fulfillment of the requirements for the degree of Master of Physics

in the

Faculty of Physics
Elementary Particle Physics

August 14, 2020

LUDWIG-MAXIMILIANS UNIVERSITÄT MÜNCHEN

MASTERARBEIT

Studien zur Zeitmessung mit dem Tile Kalorimeter für die Suche nach schweren geladenen langlebigen Teilchen mit dem ATLAS Run–2 Datensatz

---

Author:
Joschua KRINK

Supervisor:
Dr. habil. Sascha MEHLHASE

Eine Masterarbeit erarbeitet im Zuge des Master Programms in Physik

in der

Fakultät für Physik
Elementarteilchenphysik

August 14, 2020

LUDWIG-MAXIMILIANS UNIVERSITÄT MÜNCHEN

Abstract

Faculty of Physics
Elementary Particle Physics

Master of Physics

Studies on the Tile-Calorimeter Timing Measurement for a Search for heavy charged long-lived Particles in ATLAS Run–2 Data

by Joschua KRINK

Heavy charged long lived particles are predicted by many theories beyond the Standard Model. Those particles could in theory be directly observed in a particle detector. Therefore there have been multiple analyses with the ATLAS detector to search for those stable particles. As they are expected to be much heavier and therefore much slower than Standard Model particles traversing the detector, they would have quite a characteristic signature. One particular approach to detect these kind of particles is via the time-of-flight measurement in the ATLAS tile calorimeter. To be able to use that timing information and the resulting β measurement, the timing and β resolutions have to be as precise as possible.
In this thesis a calibration of the timing measurement with the ATLAS tile calorimeter is presented, using the full ATLAS Run–2 dataset of 139 fb^{-1}. Several correction and calibration steps are applied to achieve the best possible resolution. Furthermore the calibrations have been applied to a sample of simulated $Z \to \mu\mu$ events to compare the simulated timing resolution with the resolution observed in data.
Several studies on the timing measurement have been conducted to evaluate the timing performance for various conditions. The overall timing resolution could be improved by 5.3% compared to the uncalibrated resolution.

Contents

Chapter 1

Introduction

The main goal of elementary particle physics is to describe the interactions of the smallest units of which our universe is made of. Since the discovery of the first subatomic particle, the electron, in 1897 [1], physicists have continously improved their understanding of the fundamental structures of matter and forces. The most recent and definitely the most powerful of all the theories so far is the **S**tandard **M**odell of particle physics (**SM**). It provides a theoretical description of the existence and properties of elementary particles and the physical laws defining their interactions. The validation of countless of predictions made by the SM is proof for the quality of the theory so far. The last decades were filled by experimental discoveries in particle and **H**igh **E**nergy **P**hysics (**HEP**), predicted by the SM years - if not decades - in advance. Still there are phenomena in our universe which we are not able to understand to this day.

Despite all its successes, the SM lacks the power to explain many phenomena, like the existence of **D**ark **M**atter (**DM**) or the different abundances of matter and anti-matter. Therefore physicists have long been thinking of new theories, which could replicate the properties of the SM, but also enhance the range of covered physics. The searches for theories **B**eyond the **S**tandard **M**odel (**BSM**) are ongoing and have produced countless approaches to the shortcomings of the SM. Although many have been tested in specially designed experiments, no real breakthrough could be celebrated in the last few decades. Since most of the proposed theories depend on the existence of new particles, this conundrum was - and still is - the main focus of current research in particle physics.

High-energy collider experiments have been constructed to provide the possibility of creating and studying these predicted particles. The largest and most powerful particle collider is the **L**arge **H**adron **C**ollider (**LHC**) at the research facility of the **C**onseil **E**uropéen pour la **R**echerche **N**ucléaire (**CERN**) in Geneva. It habitates six experiments, including the **ATLAS** (**A** **T**horoidal **L**HC **A**pparatu**S**) detector.
The ATLAS Collaboration is currently running various searches for signs of new physics using the collision data recorded with the ATLAS detector. Many of those theories give rise to a special kind of particles, so called **L**ong **L**ived **P**articles (**LLP**s). Their lifetime is long enough to enable them to penetrate or even traverse the detector. A special breed of those LLPs are **H**eavy **C**arged **L**ong **L**ived **P**articles (**HCLLP**s), also called **S**table **M**assive **P**articles (**SMP**s). Searches for SMPs provide a model-independent method of experimentally investigating BSM physics. One characterising feature of SMPs is their unusually low velocity compared to the majority of particles produced in the collider. Therefore we can discriminate these slower particles from SM particles and focus our searches directly on SMPs. The Tile Calorimeter

(**TileCal**) is one sub-detector of ATLAS capable of measuring the velocity of traversing particles.

A so called **T**ime-**o**f-**F**light (**ToF**) measurement is used to analyse the data for SMPs. In order to provide the best possible resolution of the ToF measurement, the instrumental dependencies have to be calculated and corrected. Several dependencies can be accounted for by analysing the behaviour of muons in the TileCal. SMPs are possibly detector-stable, meaning they can travel through the whole detector leaving behind traces on their path. These traces resemble those of heavy, slow muons passing through the detector. As muons at LHC are usually produced with high energies, we can make the assumption, that they are travelling through the detector with the speed of light. Therefore we use muons from Run–2 data and **M**onte **C**arlo (**MC**) simulations to investigate the different dependencies and apply a software-based calibration to the ToF measurement. The different calibration steps are presented and explained in this thesis. Various studies on the improvement of these calibrations are conducted and analysed, with the improvements yielded being applied to the calibration.

Chapter 2

Theory

To be able to conduct a search for signs of new and unknown physics, we must first be able to understand the current state of the art. The Standard Model combines three gauge theories to provide a theoretical framework to explain most of the fundamental laws of particle physics. In this chapter, the SM particles are presented, their properties discussed and their interactions explained. In a quick overview the concepts behind forces and matter are described and examples are given.
Furthermore a short look into the open questions of the SM will be taken and different approaches to answer them will be presented. The main focus here will be on Supersymmetry (**SUSY**). Most of the information in this chapter, if not declared otherwise, are taken from [2].

2.1 Standard Model of Particle Physics

2.1.1 Elementary Particles

The Standard Model predicts the existence of 61 different elementary particles. These particles can be combined and divided into several particle groups according to their properties. The most fundamental differentiation is based on the spin of the particles. Fermions are particles with half-integer spin ($s = \frac{1}{2}\hbar$), bosons have integer spin. Fermions are also called "matter-particles", whereas bosons are the so-called "force-particles".

Fermions

Fermions are further divided into two groups: leptons and quarks. Leptons are particles with either integer electrical charge or no electrical charge at all. The word lepton[1] means light, referencing the lightweightness of leptons. They are also divided into three generations according to their mass, with each generation containing one lepton and one neutrino. The properties of the leptons can be found in table 2.1.

The second group of fermions consists of the quarks. They also carry electric charge like leptons, but in the case of quarks their electric charge is third-integer. They also carry the so-called colour charge, which enables them to take part in the strong interaction. Each quark possesses one of three possible colour charges: red, blue or green. Quarks are intend to form bound states, therefore they almost instantly connect with other quarks to form hadrons. The physical properties of the quarks can be found in table 2.2.

[1] from the greek $\lambda\epsilon\pi\tau o\chi$ leptós meaning 'light'.

TABLE 2.1: The leptons of the SM. The mass of the neutrinos could not be measured precisely so far, only upper limits can be given.

Generation	Lepton	electric charge	mass
1	electron e^-	-1e	0.511 MeV
	electron neutrino ν_e	0	< 0.12 eV
2	muon μ	-1e	105.66 MeV
	muon neutrino μ_ν	0	< 0.12 eV
3	tau τ	-1e	1.777 GeV
	tau neutrino ν_τ	0	< 0.12 eV

TABLE 2.2: The quarks of the SM.

Generation	Quark	electric charge	mass
1	up u	$\frac{2}{3}e$	2.2 MeV
	down d	$-\frac{1}{3}e$	4.7 MeV
2	charm c	$\frac{2}{3}e$	1.28 GeV
	strange s	$-\frac{1}{3}e$	96 MeV
3	top t	$\frac{2}{3}e$	173.1 GeV
	bottom b	$-\frac{1}{3}e$	4.18 GeV

There is an additional anti-particle to each of the presented leptons and quarks. The anti-particle exhibits all the same properties as its particle, but the signs of all charge-like quantum numbers are switched.

Bosons

Contrary to fermions, bosons have a spin of 0 or $1\hbar$. The particles with spin $s = 1\hbar$ are called gauge bosons. They are the exchange particles of the fundamental interactions. The W^+, W^- and Z^0 bosons mediate the weak force, the photon mediates the electromagnetic force and the gluons the strong force. There are in total 8 different gluons with different colour charges. Additionally there is one scalar boson with spin $s = 0$, the Higgs boson. The properties of the bosons can be found in table 2.3.

TABLE 2.3: The bosons of the SM.

Boson	Force	electric charge	mass	colour charge
photon γ	electromagnetic	0	0	no
W^+	weak	$1e$	80.39 GeV	no
W^-	weak	$-1e$	80.39 GeV	no
Z^0	weak	0	91.19 GeV	no
gluon g	strong	0	0	yes
Higgs H		0	124.97 GeV	no

2.1.2 Interactions

The SM is a gauge theory, which is represented by the symmetry group $SU(3)_C \otimes SU(2)_L \otimes U(1)_Y$. Three of the four known fundamental interactions are included in the SM. Only gravity could not be expressed as gauge theory so far, thus the SM is not able to describe it.

Electromagnetism (**EM**) is the oldest known of the three forces. It is described by a **Q**uantum **F**ield **T**heory (**QFT**). In the case of EM the underlying QFT is called **Q**uantum **E**lectro **D**ynamics (**QED**). The symmetry group of this gauge theory is $U(1)_{QED}$. As described above, the mediator particle of EM is the photon γ. As it is massless, the EM force is in principle infinite in range. Only particles with electric charge are able to participate in the electromagnetic interaction.
The second interaction is the weak nuclear force. It is mediated by three massive gauge bosons, the W^+, W^- and Z^0. Because of their non-zero mass, the range of the weak force is finite with the strength falling exponentially with distance. Solely left-handed particles (spin and momentum orientations are anti-parallel) are participating in the weak interaction. Its defining symmetry group is $SU(2)_L$. The weak interaction is responsible for the transformation of quarks and leptons beyond generations. Only weak processes are able to change the flavour of particles.
The third force described by the SM is the strong nuclear force. The QFT of the strong force is called **Q**uantum **C**hromo **D**ynamics (**QCD**) with the symmetry group $SU(3)_C$. It is mediated by gluons. Though gluons are massless, the range of the strong force is only about the size of a medium sized nucleus. That is due to the fact, that free colour charges cannot appear in nature above a certain distance threshold. This empirically established fact is known as confinement [3]. Therefore gluons (and also quarks) will try to form bound states with other colour-charged particles. There are two ways to form colourless bound states: All three coulours (red, green and blue) combined form the colourless state 'white', while a colour with the respective anti-colour form the colourless state 'black'.
The SM combines the weak and electromagnetic interactions to the so-called electroweak interaction, resulting in the symmetry group $SU(2)_L \otimes U(1)_Y$, where the electric charge is combined with the third component of the weak Isospin I_3 to form the hypercharge $Y = 2(Q - I_3)$.

All together, the total symmetry of the SM is represented by $SU(3)_C \otimes SU(2)_L \otimes U(1)_Y$.

The properties of the fundamental interactions contained in the SM can be found in table 2.4.

TABLE 2.4: The interactions covered in the SM. The gravitational force is not mentioned here, as it could not be described by a gauge theory so far.

Interaction	**Gauge Bosons**	**strength**	**range**
strong	gluons	1	$\sim 10^{-15}m$
EM	photon	$\sim \frac{1}{137}$	∞
weak	W^+, W^- and Z^0	$\sim 10^{-6}$	$\sim 10^{-16}$

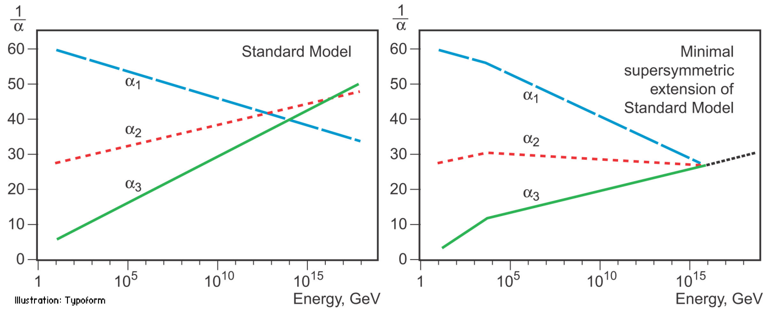

FIGURE 2.1: On the left the energy dependency of the coupling constants of the three forces described by the SM is shown. On the right the same plot for the MSSM can be seen. Figure taken from [5].

2.2 Open Questions

There are plenty of questions which cannot be answered by the SM, which indicate the need for BSM theories. Some of those questions will be discussed in short in the following, to give a quick motivation for the need of a new theory.

2.2.1 Dark Matter

Observations of the stellar motions in our universe have shown, that the combined mass of all the visible matter is not nearly big enough to explain the collected data. Also the so-called gravitational lensing hints at non-visible accumulations of matter, which can bend the light so that we see the gravitational effect of its mass. Because that mysterious matter is not interacting electromagnetically, it is called dark matter.

The SM does not predict a particle candidate with the needed properties to explain that phenomenon. Furthermore cosmological calculations have shown, that merely 4.8% of all energy in our universe is made of SM matter [4]. 26% is presumably made of dark matter. The remaining energy content is made of dark energy. Unfortunately, there is no universal theory describing the properties of dark matter and dark energy.

2.2.2 Unification of Interactions

As explained above, the SM can describe three of the four fundamental interactions. However, the couplings of these forces are not constant, but depend on the energy. As seen in figure 2.1 on the left side, there is no energy where all three coupling constants have the same value, therefore making it impossible in the SM to describe these three forces as one. With new models however, for example the **M**inimal **S**upersymmetric extension of the **S**tandard **M**odel (**MSSM**) it could be possible for the coupling constants to intersect at one point, thus clearing the way for a **G**rand **U**nified **T**heory (**GUT**).

2.2.3 Matter-Anti-Matter Asymmetry

The physical laws established by the SM treat particles and anti-particles equally, no matter their charge-like quantum numbers. It is also assumed, that the Big Bang

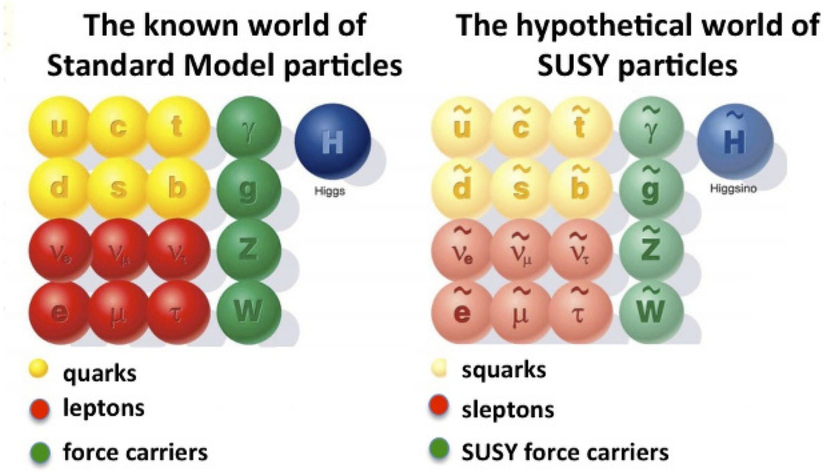

FIGURE 2.2: Figure of possible SUSY particles taken from [7].

produced equal amounts of matter and anti-matter [6]. Furthermore, the laws of relativity tell us, that every part of our universe is subject to the same fundamental laws of physics. Therefore it is odd to realise, that all of our known universe is made of matter and not anti-matter. It follows, that there must be a discriminating factor in the physical laws regarding anti-particles.
The CP-violation (**C**harge **P**arity) of the weak interaction is one means to explain that asymmetry, but its magnitude is way too low to be solely responsible for the observed imbalance.

2.3 Supersymmetry

As described in the previous section, there are some open questions to be answered. Various theories which extend the SM are trying to do so. One of the most popular BSM theories is the Supersymmetry. In the following, the main features of SUSY are presented and specific parts important for this theses are being discussed.

2.3.1 Concept

The fundamental approach of SUSY is to extend the known SM particles by so-called SUSY-particles. This happens by implying a symmetry between bosons and fermions. According to SUSY, every SM fermion has a bosonic SUSY-partner and every boson a fermionic SUSY-partner. This symmetry is constructed by the introduction of a symmetry transformation Q, which converts fermions into bosons and vice versa. This transformation can be illustrated as:

$$Q|\text{fermion}>=|\text{boson}> \quad and \quad Q|\text{boson}>=|\text{fermion}> \tag{2.1}$$

Particles which are transformed into each other are so-called superpartners and form a supermultiplet. Superpartners match in all their quantum numbers, except for the spin, which is one-half integer lower for SUSY-particles than for their SM superpartners.

TABLE 2.5: MSSM particles adapted from [8].

Names	spin	Gauge Eigenstates	Mass Eigenstates
squarks	0	$\tilde{u}_L$, $\tilde{u}_R$, $\tilde{d}_L$, $\tilde{d}_R$ $\tilde{s}_L$, $\tilde{s}_R$, $\tilde{c}_L$, $\tilde{c}_R$ $\tilde{t}_L$, $\tilde{t}_R$, $\tilde{b}_L$, $\tilde{b}_R$	same same $\tilde{t}_1$, $\tilde{t}_2$, $\tilde{b}_1$, $\tilde{b}_2$
sleptons	0	$\tilde{e}_L$, $\tilde{e}_R$, $\tilde{\nu}_e$ $\tilde{\mu}_L$, $\tilde{\mu}_R$, $\tilde{\nu}_\mu$ $\tilde{\tau}_L$, $\tilde{\tau}_R$, $\tilde{\nu}_\tau$	same same $\tilde{\tau}_1$, $\tilde{\tau}_2$, $\tilde{\nu}_\tau$
neutralinos	$\frac{1}{2}$	$\tilde{B}^0$, $\tilde{W}^0$, $\tilde{H}_u^0$, $\tilde{H}_d^0$	$\tilde{N}_1$, $\tilde{N}_2$, $\tilde{N}_3$, $\tilde{N}_4$
charginos	$\frac{1}{2}$	$\tilde{W}^\pm$, $\tilde{H}_u^+$, $\tilde{H}_d^-$	$\tilde{C}_1^\pm$, $\tilde{C}_2^\pm$
gluino	$\frac{1}{2}$	$\tilde{g}$	same
gravitino	$\frac{3}{2}$	$\tilde{G}$	same

The naming of these new SUSY particles has been quite pragmatic. The bosonic superpartners of a SM fermion were given a prefix 's', indicating it as a scalar particle. The fermonic superpartner of SM bosons were given a suffix 'ino'. For example the superpartner of the electron is called selectron, that of a gluon is called gluino. In notations, the superpartners are given a tilde '$\sim$' to indicate it as a SUSY particle.

SUSY therefore accounts for at least the same amount of new particles as already present in the SM. In the MSSM, which by definition is the minimal extension of the SM, even more than that amount of new particles are introduced.
The Higgs boson gets four superpartners instead of just one. The electroweak gauge bosons also get more than just one superpartner. This is caused by the different mixings of the gauginos and higgsinos. Four neutral mass eigenstates are created by the mixing of the electrically neutral gauginos and the higgsinos; the so-called neutralinos. Likewise the electrically charged gauginos and the higgsinos mix into four electrically charged 'charginos'. The full particle content of the MSSM is presented in table 2.5.

We now know the particles that the MSSM predicts and should be able to search for them in collider experiments. But so far, no SUSY particle was found. In theory, these sparticles should have the same masses as their SM partners, but that cannot hold, for we have not seen a SUSY particle yet. Therefore SUSY must be broken. We can assume the masses of the sparticles to not be many magnitudes higher than those of the SM particles. Otherwise further problems would occur.

2.3.2 R-Parity

Another feature of SUSY models is the possibility of lepton or baryon number violation. But that is in vast conflict with the stability of the proton. Therefore a new conversation law is introduced: the R-parity conservation.

R-parity is defined as

$$P_R := (-1)^{3(B-L)+2s} \tag{2.2}$$

where B is the baryon number, L is the lepton number and s is the spin of the particles. The R-parity is always $P_R = +1$ for SM particles and $P_R = -1$ for SUSY particles. Furthermore R-Parity is a multiplicative quantum number, meaning $(-1) \cdot (-1) = +1$ and $(-1) \cdot (+1) = -1$. Some SUSY models require R-Parity to always be conserved, whereas other models allow for R-Parity violation. If R-Parity is indeed conserved, a SUSY particle would always need to decay in at least one other sparticle, which would make the **L**ightest **S**upersymmetric **P**article (**LSP**) stable and therefore a good candidate for dark matter.

2.4 Longevity

As the background of this thesis is a search for long-lived particles, it is necessary to introduce the concept of the lifetime of a particle to understand the concept of LLPs. The most important concept to grasp is that the lifetime of particles is statistical in nature. That means, that the same kind of particle can decay in a range of decay-times. The lifetime is defined as the time it takes for a sample to decay so that a fraction of $1/e$ is left ($\sim$ 37%). After two lifetimes, $1/e^2$ would be left and so on. The stochastic process underlying the decay of particles is following the function

$$N(t) = N_0 \cdot e^{-\frac{t}{\tau}} \tag{2.3}$$

with $N(t)$ the amount of particles after a time t, N_0 the original amount of particles, t the sample time and τ the mean lifetime of the particles as explained above. The mean lifetime is anti-proportional to the total decay rate Γ_{total} as

$$\Gamma_{total} = \frac{1}{\tau}. \tag{2.4}$$

A particle, however, cannot only decay in one single way, but often via several decay channels. Each decay channel has a certain decay rate, which can be calculated via Fermi's Golden Rule:

$$\Gamma = \frac{(2\pi)^4}{2M} S \int |\mathcal{M}|^2 \delta^4 \left(P - \sum_{i=1}^{n} p_i \right) \prod_{i=1}^{n} \frac{d^3\vec{p}_i}{(2\pi)^3 2E_i}. \tag{2.5}$$

Here, M is the mass of the decaying particle, S a statistical factor, $|\mathcal{M}|$ the Matrix element accounting for this characteristic decay process, P the four-momentum of the particle and p_i and E_i the four-momentum and the Energy of the decay products. The total decay rate for a particle can then be calculated by summing up the single decay rates of each channel:

$$\Gamma_{total} = \sum_{i=1}^{n} \Gamma_i \tag{2.6}$$

The question now arising is, what physical properties account for a long lifetime? Some factors can directly be found by looking at equation 2.5 and 2.6:

- The strength of the coupling is a big factor in determining the lifetime of a particle. As seen in table 2.4, the strength of the different interactions varies greatly. This property is accounted for in the matrix element $|\mathcal{M}|$. Decays via the strong interaction have a much larger coupling than e.g. decays via the weak interaction, leading to a much smaller decay rate and therefore longer lifetime of weak decays.

- Almost conserved quantum numbers: There is a set of quantum numbers, such as the lepton or baryon number, which are mostly conserved in certain decays. That leads to a strong suppression of decays violating said quantum numbers. The matrix element also accounts for this property.
- The phase space $\int \prod_{i=1}^{n} d^3\vec{p}_i$: Depending on the mass and energy of the decay products, the phase space differs and therefore influences the decay rate.
- As seen in Equation 2.6, the total decay rate depends on the number of possible decays. Therefore a smaller amount of decay channels can lead to a longer lifetime.
- If the intermediate particle in the decay has a large mass, the probability for the decay is rather low, leading to a longer lifetime.

Chapter 3

Experimental Setup

3.1 Large Hadron Collider

The **L**arge **H**adron **C**ollider **LHC** is the worlds largest hadron collider with a circumference of 26.7 km. It is located at CERN near Geneva, in Switzerland. Originally the tunnel of the LHC was build for and used by the **L**arge **E**lectron **P**ositron (**LEP**) collider. LEP was in use from 1989 till 2000. The LHC was put into operation on 10 September 2008 and is the latest part of the CERN accelerator complex to this date [9].

The collider ring itself is made of eight straight sections and eight arcs. It contains two beam pipes, which intersect at four points, at which the experiments are localised [10](see Figure 3.1). In these beam pipes, the projectile particles are accelerated in opposite directions. The LHC accelerates hadrons, mainly protons, but also heavy nuclei like lead ions. To be able to keep these charged particles on their trajectories, 1232 superconducting dipole magnets are used. They are situated at the eight arcs of LHC. These dipole magnets can produce a magnetic field of 8.33 T. To be able to create such powerful magnetic fields, the magnetic coils are cooled down to below 2 K, using superfluid helium. To focus the beams, quadrupole or even higher multipole magnets are used.

To accelerate protons to almost the speed of light, multiple pre-accelerators come into action. In total, four pre-accelerators are supplying the LHC with high-energy protons. The first acceleration is done by LINAC2, which boosts protons to 50 MeV. After that, the Proton Synchroton Booster and the Proton Synchroton accelerate the protons to 1.4 GeV and then 26 GeV, respectively. The last pre-accelerator is the Super Proton Synchroton, which ultimately provides the LHC with 450 GeV protons. A graphic display of the CERN accelerator complex can be seen in Figure 3.2. After being injected into the LHC, the protons are finally accelerated to their maximum energy, which is designed to be up to 7 TeV. The data used in this thesis, however, was produced with a centre-of-mass energy of 13 TeV, meaning that the final proton energy was 6.5 TeV.

Protons are, however, not accelerated as single particles, but in bunches of $1.15 \cdot 10^{11}$ protons per bunch. There are 2500 bunches per beam with a time spacing of 25 ns between them. The measurable for the number of collisions that can be produced per cm^2 and per second is called the **Luminosity** $\mathcal{L}$.

$$\mathcal{L} = \frac{N_b^2 n_b f_{rev} \gamma_r}{4\pi\epsilon_n\beta^*} \cdot F \tag{3.1}$$

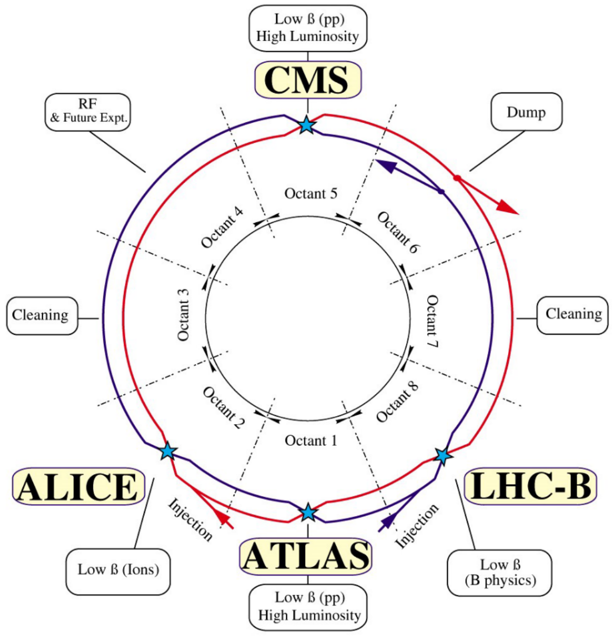

FIGURE 3.1: The LHC collider ring, showing a the intersection point of the beam pipes where the big experiments are located [10].

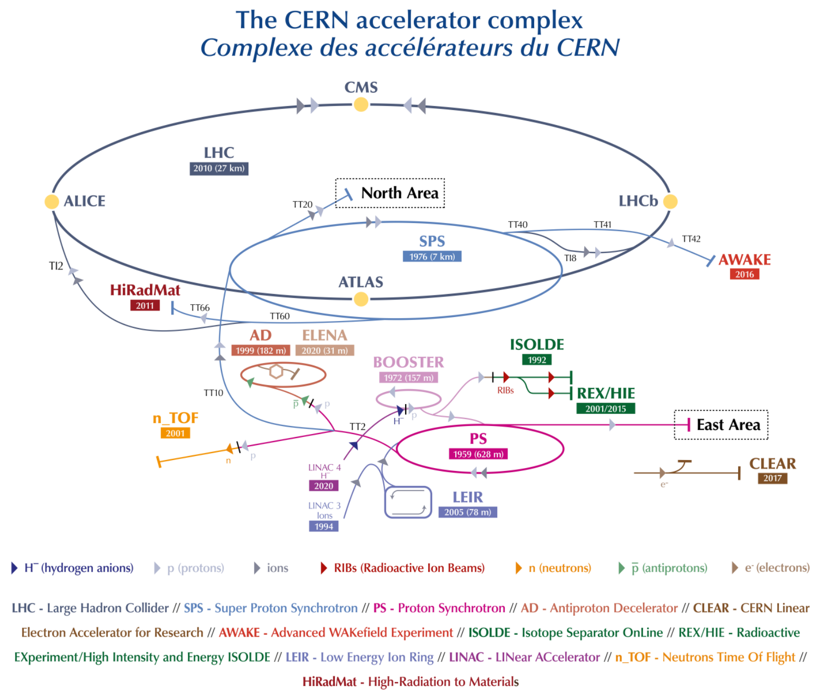

FIGURE 3.2: A schematic image of the accelerator complex located at CERN. The figure was taken from [11].

N_b is the aformentioned number of protons per bunch, n_b the number of bunches per beam, f_{rev} the rotation frequency of the proton bunches and γ_r the Lorentz factor. In the denominator, ϵ_n is the normalized beam emittance and β^* the beta-function, which is a measure for the size of the particle beam. Finally, F is a geometric factor accounting for the crossing angle of the beams at the point of interaction. The designed peak luminosity of LHC was about $10^{34}\text{cm}^{-2}\text{s}^{-1}$, which was surpassed in Run 2 by a factor of 2 [12].

As mentioned before, there are four intersection points of the beam pipes where experiments, namely particle detectors are located. In total, there are seven detector-based experiments at LHC, with the four main experiments being **ATLAS**, **CMS** (**C**ompact **M**uon **S**olenoid), **ALICE** (**A** **L**arge **I**on **C**ollider **E**xperiment) and **LHCb** (**L**arge **H**adron **C**ollider **b**eauty). ALICE and LHCb are detectors specialized for the exploration of specific phenomena. In ALICE's case, the detector is designed to study strongly interacting matter at extreme energy densities and the properties of a phase called quark-gluon plasma [13]. LHCb on the other hand, is designed to study the properties of the second heaviest of the quarks, the so-called 'bottom quark' (often just called 'b quark' or 'beauty')[14].
CMS and ATLAS, however, are general-purpose detectors designed to investigate a range of physics as broad as possible. They are constructed in such a way, that they are able to cross-confirm any discoveries made by each other. In this thesis, only data from the ATLAS detector was used, therefore a closer look at this experiment will be taken.

3.2 ATLAS Detector

ATLAS is a multi-purpose detector constructed to identify and measure certain properties of as many of the particles produced in proton-proton collisions as possible. To be able to detect different kinds of particles, ATLAS is build in circular layers around the **I**nteraction **P**oint (**IP**). Therefore it consists of several sub-detectors, all tasked with different purposes. In the following subsections, these sub-detectors will be introduced and described, with the focus being on the subsystem of relevance to the analysis presented here. But first the special ATLAS coordinate system will be explained.

3.2.1 ATLAS Coordinate System

For being able to precisely measure the spatial properties of particle tracks and interactions of traversing particles with the detector, it is necessary to introduce a geometric coordinate system. At ATLAS, a right handed coordinate system is used, with the interaction point serving as its origin. The z-axis is pointing in counter-clockwise beam direction, the x-axis towards the collider rings centre and the y-axis is pointing upwards [15]. Because of the cylindrical shape of the ATLAS detector, a cartesian coordinate system is not always of the best use. Therefore, spherical coordinates are also introduced. The azimuthal angle ϕ is measured in the x-y-plane around the beam line and the polar angle θ is calculated from the beam line. The distance from the interaction point is defined as

$$d := \sqrt{x^2 + y^2 + z^2} \tag{3.2}$$

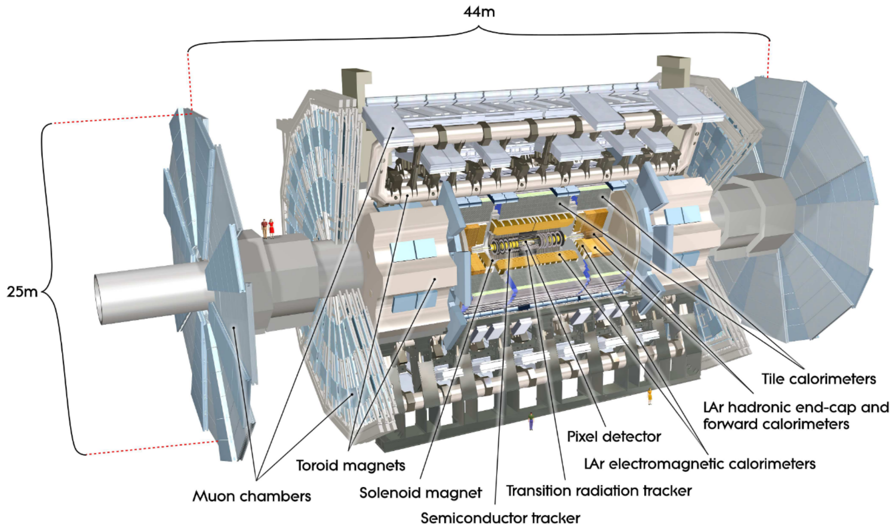

FIGURE 3.3: The ATLAS detector showing the main sub-detectors. Figure taken from [17].

For practical use though, a different set of coordinates is used. In the transverse plane, cylindrical (r, ϕ) coordinates are used with

$$r := \sqrt{x^2 + y^2} \tag{3.3}$$

As opposed to the polar angle θ the pseudorapidity η is used, being defined as

$$\eta := -ln[tan(\theta/2)] \tag{3.4}$$

The advantage of using the pseudorapidity η is, that the particle production turns out to be approximately constant as a function of η [16].

3.2.2 Inner Detector

The **I**nner **D**etector (**ID**) is the innermost part of ATLAS, directly surrounding the beam pipe. It is comprised of three complementary sub-detectors all immersed in a magnetic field of 2 T parallel to the beam axis [18]: The Pixel Detector, the Semiconductor Tracker and the Transition Radiation Tracker. Its main purpose is to reconstruct the path of traversing particles. Because of the magnetic field, the tracks of charged particles are bent, so that it is possible to calculate their momentum from the curvature. Furthermore, the **P**rimary **V**ertex (**PV**) is reconstructed and the spatial difference between the PV and the Interaction Point can be calculated. That is especially important as displaced vertices are hints for LLPs. The layout of the complete ID can be seen in Figure 3.4.

The Pixel Detector as the innermost part of the ID is a high granularity silicon detector with 80 million pixels spanning an area of 1.7m^2. It has a resolution of 14 x 115μm^2 at a pixel size of 50 x 400μm^2 [18]. The pixel detector can be used for a measurement of the ionisation energy loss which will be discussed in more detail in Chapter 4.

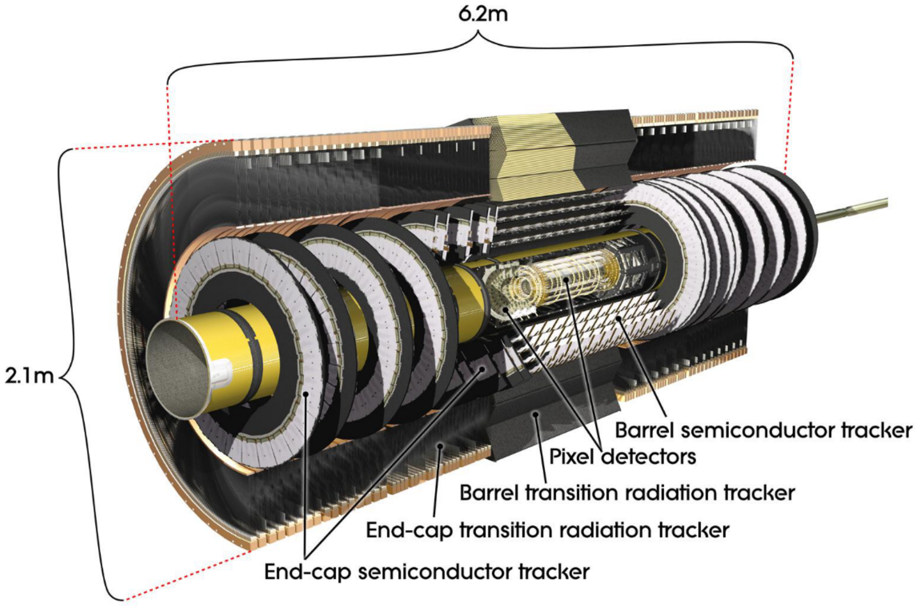

FIGURE 3.4: The ATLAS Inner Detector showing the different sub-systems. Figure taken from [20].

The intermediate sub-detector is the Semiconductor Tracker, a silicon microstrip tracker consisting of 4088 two-sided modules with over 6 million read-out channels. It provides ultra-precise position measurement due to the small size of the stripes with an accuracy of 17μm per layer in the direction transverse to the stripes.
The third part of the ID is the **T**ransition **R**adiation **T**racker (**TRT**). The TRT uses straw tubes with a diameter of 4 mm as basic detector elements, which provide a precision measurement with a spatial resolution of 0.17 mm. The TRT also provides additional information about the traversing particle as it can distinguish between normal particle hits and transition radiation [19].

3.2.3 Electromagnetic Calorimeter

The **E**lectromagnetic **Cal**orimeter (**ECal**) is situated around the ID of ATLAS. As a calorimeter, its main purpose is the measurement of the energy traversing particles deposit in the different cells as they are passing through the detector. It is specifically designed to stop and absorb the electromagnetic particles produced in the interaction, namely electrons, positrons and photons. Although it can also detect different particles, its main focus is on these three. High energy electrons and positrons emit bremsstrahlung while passing through the ECal. These photons then undergo pair-creation in the presence of the detector material's nuclei and produce an electron-positron pair. In each of these processes, the amount of particles double, while each single particle is losing energy. If the energy of a single particle falls below a certain threshold where the ionisation energy loss takes over, the particles get absorbed by the detector. This process is called showering. The depth of the shower is described in multiples of the radiation length, which itself is defined as the mean distance over which an electron has its energy reduced to 1/e of its initial energy [21].
The ECal is designed to measure the whole shower and therefore has a minimum

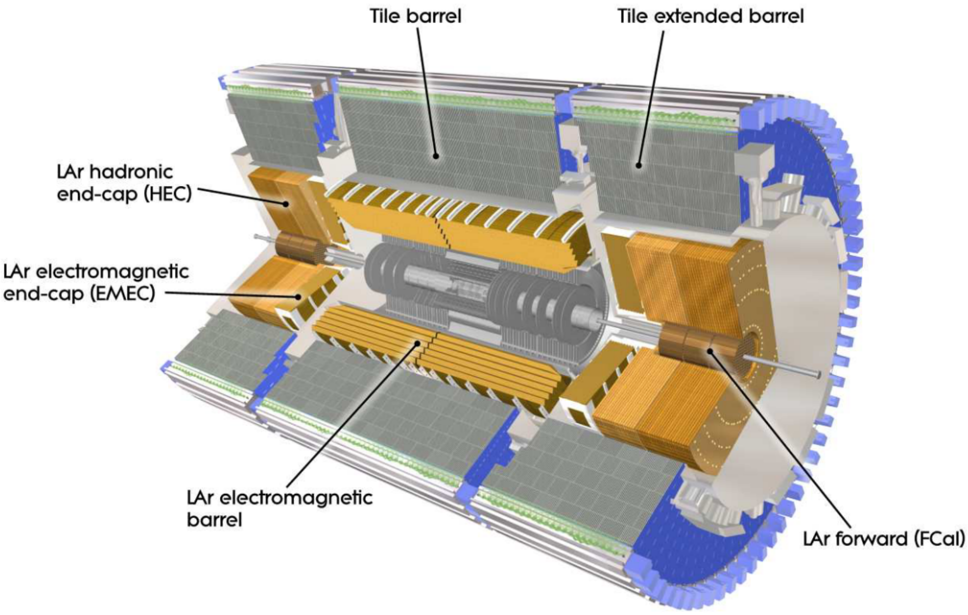

FIGURE 3.5: The ATLAS calorimeter showing the electromagnetic and hadronic barrels, as well as the end-caps and forward calorimeters. Figure taken from [23].

thickness of 22 radiation lengths [22].
Furthermore, the ECal is constructed as a sampling calorimeter, meaning it consists of layers of two different materials: an absorber and an active material. For the ECal of ATLAS, lead is used as absorber material and **L**iquid **Ar**gon as active medium, giving the ECal the often-used name LAr calorimeter. The different layers in the barrel region are arranged in an accordion shape, giving the LAr a seamless design in ϕ-direction. A schematic picture of the ATLAS calorimeters can be found in Figure 3.5.

3.2.4 Hadronic Calorimeter

Just like the ECal, the **H**adronic **Cal**orimeter (**HCal**) is designed to measure the energy and stop particles passing through the detector. But in this case, it's a calorimeter constructed for the measurement of hadrons. The barrel region of the HCal is often reffered to as **Tile Cal**orimeter (**TileCal**). Hadrons are compound particles, consisting of usually two or three quarks (see Section 2.1.1). Therefore, the showering mechanism works differently than in the ECal. The leading processes in hadronic showers are hadron production, nuclear de-excitation and pion and muon decays. Hadronic showers typically are longer than electromagnetic, hence the density of the HCal needs to be higher. The HCal consists of the TileCal in the barrel and extended barrel region and a LAr hadronic calorimeter in the end-caps and the forward calorimeters. The barrel covers the region of $-1.65 < \eta < 1.65$, while the end-caps cover the region for $1.5 < |\eta| < 3.2$ and the forward calorimeters take the range between $3.1 < |\eta| < 4.9$. This translates to a coverage of almost 4π [24]. The TileCal is made of steel as absorber and scintilation tiles as active medium. The barrel part is 5.64 m in length along the beam axis, while the extended barrel cylinders span 2.91 m on each side [24]. The detector cylinder is made of 64 independent wedges

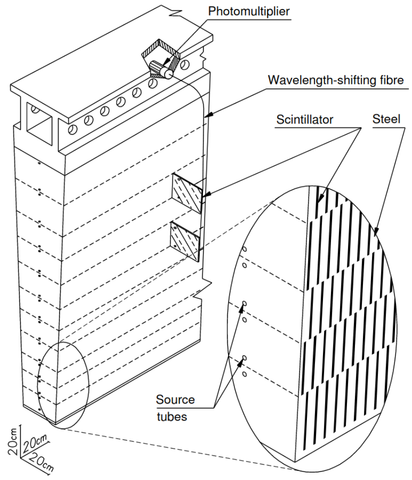

FIGURE 3.6: The Geometry of the wedges of the Tile calorimeter. Figure taken from [25].

along the azimuthal direction. Each wedge covers a range of 0.1rad in ϕ. The cells in the plane spun by r and z have an η-coverage of 0.1 in the inner two layers, while the cells in the outer layer cover a range of 0.2 in η. The radial depth of the TileCal is approximately 7.4λ [25]. In this case, the depth is measured in interaction lengths, as opposed to the radiation length for the ECal.
The wedges form an almost-periodic steel-scintillator structure, which is ordered with a ratio by volume of approximately 4.7 : 1 [25]. A sketch of this geometry can be found in Figure 3.6.

The different layers of the calorimeters are called samplings and are numbered. For this thesis, only the samplings 12 to 20 in the TileCal are of importance. The shape of the cells in samplings 12 to 20 can be found in Figure 3.7. The cells are also numbered according to their placement in the calorimeter. As the TileCal is circular, the size of the cells differ significantly. The innermost cells are as small as 25cm x 25cm, while the outermost cells can have a size of around 1m x 1.5m. That size difference will be of importance in the later parts of this thesis. But not only the size, also the shape of the cells vary. While most of the cells are rectangular in the r-z-plane, the middle layer of the TileCal, sampling 13, contains cells with a shape of two rectangles on top of each other, shifted in z-direction.

Due to the orientation of the scintillator tiles and the use of wavelength-shifting fibre readouts on the tile edges, an almost seamless azimuthal calorimeter coverage can be achieved. The layout of the readout fibres into the photomultiplier tubes provides an approximately projective geometry in η. The electronic read-outs are producing two different pulses: a low and a high gain pulse. This splitting provides a large dynamic range and is also beneficial towards a good signal-to-noise ratio [26]. Finally, the energy resolution of the barrel and end-cap calorimeters is

$$\frac{\sigma_E}{E} = \frac{50\%}{\sqrt{E[GeV]}} \oplus 3\%. \tag{3.5}$$

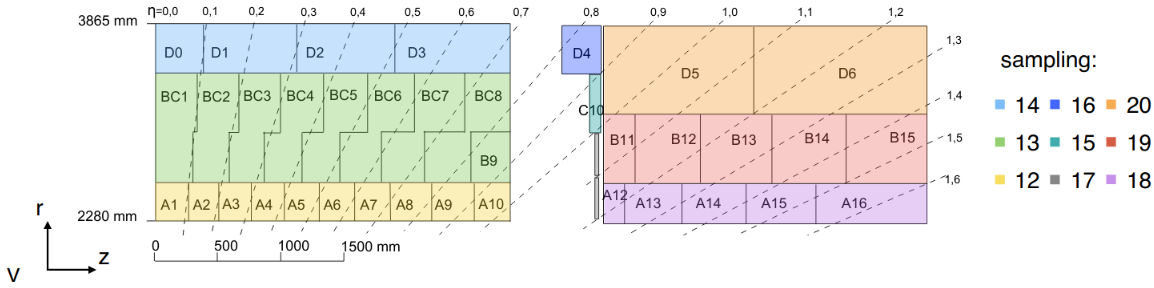

FIGURE 3.7: The Tile calorimeter cells and their naming scheme. Figure taken from [26].

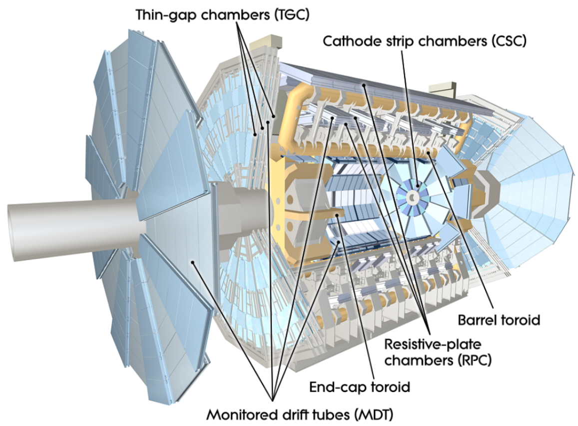

FIGURE 3.8: The Muon Spectrometer and its sub-systems. Figure taken from [29].

3.2.5 Muon Spectrometer

The **M**uon **S**pectrometer (**MS**) is the outermost part of the ATLAS detector. It is designed as a tracking detector, similar to the inner detector, with the purpose of measuring the tracks of particles passing the calorimeters. Therefore, a set of three toroidal magnets is installed between the HCal and the MS [27]. Each of the magnets is made of eight coils. The strength of the bending of the particle track is different, depending on the η value of the track.
The MS is made of several sub-systems. The **T**hin **G**ap **C**hambers (**TGC**), the **R**esistive **P**late **C**hambers (**RPC**), the **M**onitored **D**rift **T**ubes (**MDT**) and the **C**athode **S**trip **C**hambers (**CSC**).
The MDTs provide a high precision measurement of the track over most of the η-range. There are 1,171 chambers with a total of 354,240 tubes, which achieve a resolution of 80μm per tube. In the end-cap region for large η values the coordinates of the track are measured by the CSCs. They can even reach a resolution of 60μm [28].
The RPCs are designed for triggering and a second coordinate measurement in the central region. In the end-cap region, the same task is executed by the TGCs. An illustration of the MS with an indication of the several parts can be found in Figure 3.8.

Chapter 4

Search for Heavy Charged Long-Lived Particles

In this chapter, the general motivation for the search for HCLLPs is set out. Their production in collider experiments is discussed and examples are given. As further motivation for the main part of this thesis, the main observables for the analysis are given.

4.1 Motivation

Many theories beyond the standard model are predicting the existence of HCLLPs. For this thesis, these particles are defined to be detector stable and are expected to travel with a velocity significantly slower than the speed of light ($\beta\gamma \leq 0.9$ [30]). As they are detector stable, they are in theory able to directly interact with the detector material, leaving behind very characteristic signatures. Because their mass is much bigger and their velocity much slower than that of the SM particles able to traverse and interact with the detector, there is basically very little to no SM background.
Also, different BSM theories predict different physical properties such as particle masses and coupling constants for each model. This requires specific analyses for different theories and parameter sets. As various BSM theories include HCLLPs, the search for those is designed to be rather model independent, paving the way for broader analyses.

4.2 Production of HCLLPs

New long-lived particles are thought to be produced in pairs at colliders [31]. That is due to the assumption, that there will be some quantum number conservation in the BSM theory (see Chapter 2.3.2) in which the new particles occur. As their production is influenced by the existence of that (almost) conserved quantum number, also their decay will be suppressed. That results in their longevity, leading the way to the possibility of a direct interaction within the detector as an SMP.
Another reason for the preferred production in pairs is the direct proportionality of the production cross section to the decay width:

$$\sigma(ab \rightarrow X) \propto \Gamma(X \rightarrow ab) \tag{4.1}$$

This means, that for a singly produced particle X with a lifetime long enough to penetrate through the detector, its production rate would be almost negligible, as the lifetime is directly proportional to the inverse of the decay width [31].

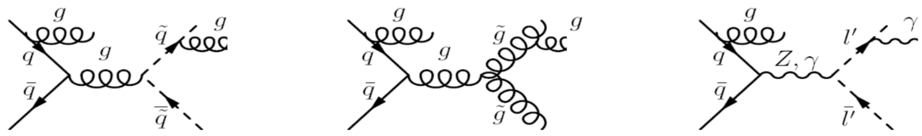

FIGURE 4.1: Examples of Feynman diagramms for the leading production mechanisms for long-lived particles. The shown processes are squark-anti-squark pair-production (left), gluino production (middle) and slepton-anti-slepton production via quark anti-quark annihilation. The figure was taken from [31].

HCLLPs could also be produced by the decay of a heavier particle into a lighter state, which then cannot decay (rapidly) any further.

Examples for production mechanisms can be seen in Figure 4.1

4.3 Observables

4.3.1 Ionisation Energy Loss

One particular interesting observable for the identification of particles is $\langle \frac{dE}{dx} \rangle$, the specific ionisation energy loss. When a charged particle is interacting with the detector, it loses energy due to the ionisation of the atoms in the detector material. To be more precise, the traversing particle is interacting with the electrons of the atoms, exciting or ionizing them [32]. The mean energy loss is then given by

$$\left\langle \frac{dE}{dx} \right\rangle = \frac{4\pi e^4 z^2}{m_e c^2 \beta^2} n \left(\frac{1}{2} ln \left(\frac{2 m_e c^2 \beta^2 \gamma^2 T_{max}}{I_e^2} \right) - \beta^2 - \frac{\delta}{2} \right). \tag{4.2}$$

This relation is called the Bethe-Bloch-formula [32]. Here, e is the elementary charge, z the charge of the traversing particle in multiples of e, m_e the mass of an electron and n the volume density of electrons in the detector material. Furthermore, c is the speed of light, $\beta := \frac{v}{c}$ the velocity of the projectile particle in relation to c and γ is the Lorentz factor defined as

$$\gamma = \frac{1}{\sqrt{1-\beta^2}}. \tag{4.3}$$

I_e describes the mean ionisation potential, δ is a material constant accounting for density effects and T_{max} is the maximum energy transfer a electron can receive in a collision. For particles much heavier than an electron, this is given by

$$T_{max} = 2 m_e c^2 \beta^2 \gamma^2. \tag{4.4}$$

As can be seen in Equation 4.2, the $\langle \frac{dE}{dx} \rangle$ measurement is only dependent on material specific quantities and the speed of the projectile particle. Therefore $\langle \frac{dE}{dx} \rangle$ can be used for a $\beta\gamma$ estimation. Together with the momentum measurement received from the bending of the track in the magnetic field of the inner detector, a mass calculation can be done using

$$m_{\beta\gamma} = \frac{p}{\beta\gamma}. \tag{4.5}$$

As HCLLPs are much heavier than SM particles, their specific ionisation energy loss is very characteristic. The pixel detector of the ID is ideally suited for a $\langle\frac{dE}{dx}\rangle$ measurement. It is the first part of ATLAS with which the particles can interact and its $\langle\frac{dE}{dx}\rangle$ resolution is a lot higher than that of the TRT [33].

However, particles will not deposit all their energy in one layer of the pixel detector. Therefore, to get a good $\langle\frac{dE}{dx}\rangle$ estimate, it is crucial to average over all measurements in the different layers. The averaging yields the **M**ost **P**robable **V**alue (**MPV**) which differs from the mean value given by Equation 4.2 as $\langle\frac{dE}{dx}\rangle$ is Landau distributed. So an empiric Bethe formula with three parameters is used to connect the measured $\langle\frac{dE}{dx}\rangle$ values with the particle's velocity β:

$$MPV_{\frac{dE}{dx}}(\beta\gamma) = \frac{A}{(\beta\gamma)^C} + B \tag{4.6}$$

The values of the three parameters A, B and C are measured using low-momentum pions, kaons and protons. The $MPV_{\frac{dE}{dx}}$ is extracted from a fit to the distribution of $\langle\frac{dE}{dx}\rangle$ values for each particle species [30].

The final $\beta\gamma$ estimate can then be obtained by inverting equation 4.6.

4.3.2 Time-of-Flight Measurement

Another observable for the search for HCLLPs is the measurement of the ToF in the TileCal or the MS. The ToF measurement in the TileCal will be covered in detail in the following chapters, so only a quick overview of the principles will be presented here.

As HCLLPs have a much larger mass than SM particles traversing the detector, given the same energy and momentum, they will travel with a much lower velocity. Therefore they will arrive much later at a distance d in the outer detectors of ATLAS. That time difference can be used to identify HCLLPs.
To quantify that time difference, the variable t_0 is introduced. It is defined as the difference between the actual time-of-flight ToF_a and the time-of-flight ToF_c a particle with $v = c$ would need:

$$t_0 = ToF_a - ToF_c = ToF_a - \frac{d}{c} \tag{4.7}$$

Using t_0, the β-value of the HCLLP as the main observable can be calculated as

$$\beta = \frac{d}{d + t_0 \cdot c}. \tag{4.8}$$

Chapter 5

Time-of-Flight Measurement in the ATLAS Tile Calorimeter

The purpose of this section is to explain the calibration of the timing measurement in the ATLAS TileCal. In order to achieve the best possible timing resolution, various calibration steps have been implemented to correct for mismeasurements and dependencies on different variables. For the calibration, the timing resolution is tested using muons in data and MC simulation. For data, the whole ATLAS Run–2 dataset was used, amounting to a total of 139 fb^{-1} of proton–proton collision data (total of 1,540,451,320 events) at a centre-of-mass energy of 13 TeV usable for physics [34]. For MC, a sample of simulated $Z \rightarrow \mu\mu$ events consisting of 155,981,912 events was used.

5.1 Pre-Selections

As the signature an HCLLP would leave in the detector resembles that of a heavy muon, they are the obvious choice to use for the calibration. Muons which are produced in proton–proton collisions in the ATLAS detector usually are travelling with velocities so close to the speed of light that we cannot resolve the difference. Therefore we can assume that

$$v_\mu = c \quad \rightarrow \quad \beta_\mu = 1 \tag{5.1}$$

for all muons used for the calibration.

For being used in the calibration, some requirements are set for the muons:

- Muons are required to have a p_t of at least 25 GeV. That is partly due to the efficiencies of the muon reconstruction [35]. Another reason is the fact, that muons with a momentum larger than 25 GeV are already in the relativistic rise of the Bethe-Bloch-Formula (see Equation 4.2). That means their energy deposit is larger than the minimum, leading to a smaller amount of cell hits lost to the minimum E_{Hit} requirement.
- The links between different representations of the muon in the detector and the link to the primary vertex have to be valid.

Furthermore, there are several requirements for the cell hits and the data itself for them being used in the calibration:

- Cells hit in the TileCal by muons are required to be associated with a Track in the ID. Cells are counted as associated, if an extrapolation of an ID track is passing through them. An association with an ID track is of great importance, as various properties measured in the ID, such as the transverse momentum p_t or the spacial properties of the track are used as pre-selections or later in the calibrations.

- Only TileCal cells with a minimum energy deposit $E_{Hit} \geq E_{Hit_{min}}$ are used for the calibration. That requirement is meant to reduce the effects of detector noise, originating from the electronics of the TileCal. For the calibration a minimum energy deposit per cell of $E_{Hit_{min}} = 500$ MeV is required. Further, the effects of different, lower $E_{Hit_{min}}$ requirements are tested and the results are presented.

- As the LHC is filled with a bunch of protons every 25 ns, $|t_0|$ is required to be less than 25 ns to reduce the amount of cell hits originating from the previous or the following bunch crossing.

- All used data events have to be recorded while the detector was fully functional and ready for data-taking. To ensure that, a Good-Runs-List for the full Run–2 data has been used.

- Specific cells in the TileCal, showing unexpected measurement results or failing to achieve the required conditions for statistics, are not taken into account for the ToF measurements.

For the $Z \rightarrow \mu\mu$ selection applied to MC simulated events, further pre-requisites are required for the muons:

- Exactly two muons have to be in the event, as per definition we require the event to be a Z-boson decaying to two muons.

- To ensure, that these two muons originate from the Z decay, we require them to have opposite charge.

- Their invariant mass must differ no more than 10 GeV from the Z-boson mass of 91.1876 GeV [36].

5.2 Calibrations

The main body of this thesis, several calibrations to achieve the best possible timing resolution with the TileCal, is now presented. The complete calibration consists of multiple steps applied in a certain order. That order of calibrations was adopted from an earlier calibration using a dataset from the first half of Run–2 [26]. The results yielded by changing the order of calibrations is presented in Chapter 6. The different calibration steps are:

- First, a geometrical *distance correction* is applied, correcting the length of the travelled distance from the IP to the TileCal cell according to the tracks spacial properties.

- Following that, an *η-calibration* is exercised, ensuring a consistent measurement over the full η range of the TileCal.

- We expect the TileCal properties to be symmetric in ϕ. To ensure that symmetry and calibrate for any possible discrepancies, a *ϕ-calibration* is applied, simmilar to the *η-calibration* before.
- As the timing resolution depends on the deposited E_{Hit} in the respective TileCal cell, an *energy calibration* is done, adjusting for any energy-correlated biases.

These calibrations are applied to data as well as to MC simulation. They account for potential asymmetries in the overall t_0 distributions. For data, two further calibration steps are applied:

- A *cell-wise calibration* is ensuring a stable timing measurement for all single TileCal cells.
- A *run-wise calibration* is calibrating any biases depending on the time of data-taking.

As those biases are not implemented in simulation, theses calibration steps are not applied to MC simulation. However, the simulated t_0 distribution is smeared to account for differences in the simulated and observed timing resolution. The dependency of the timing resolution on the deposited energy in simulation differs to that in data, therefore an *energy-based smearing* is applied.
As last step, a *pull correction* is applied separately for data and simulation.

We expect the properties of all ϕ-wedges with the same r and z values to be uniform, therefore we expect the same biases in each of these cells. To increase the statistics and therefore hopefully the quality of the calibrations, all of the calibration steps, except of course the cell-wise step, are performed using the so-called *ϕ-projected cells*. For one ϕ-projected cell, all TileCal cells of one type with the same r and z properties are taken together.

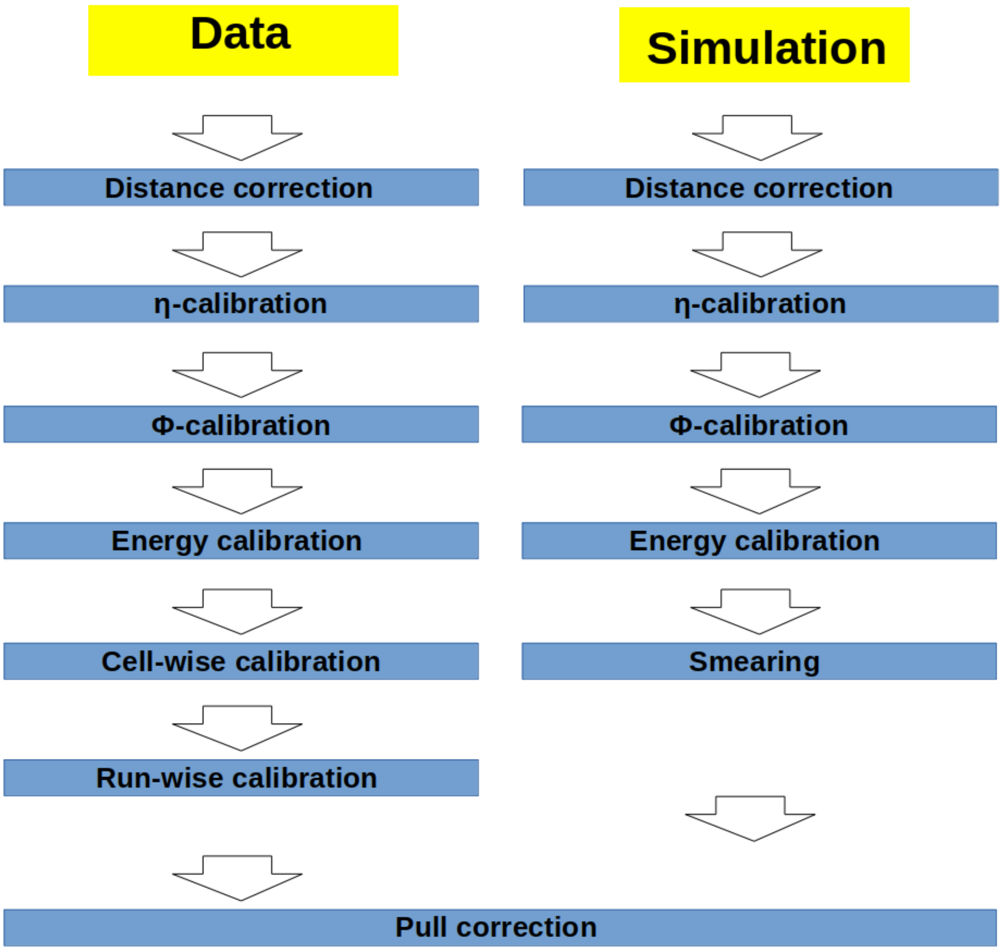

FIGURE 5.1: The order of the steps for the TileCal timing calibration.

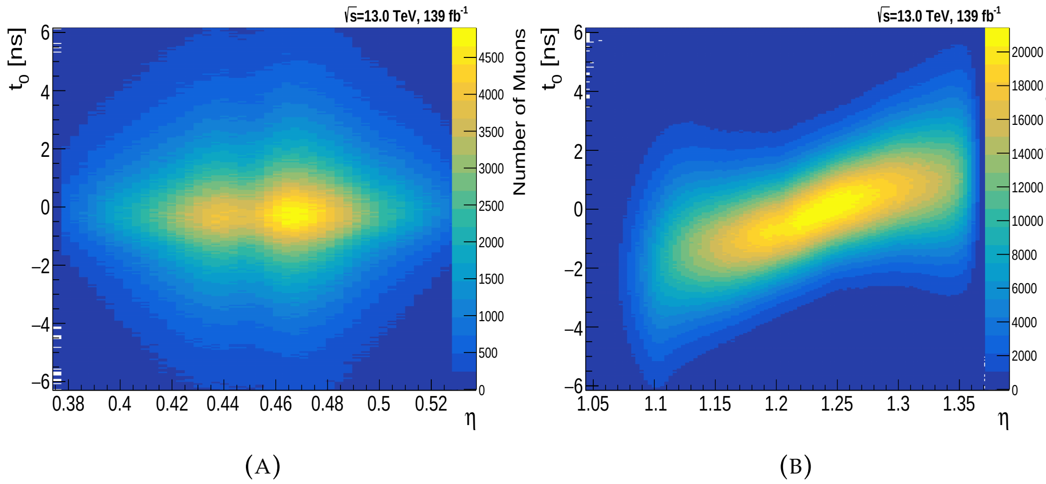

FIGURE 5.2: The dependency of the t_0 measurement on η for two different TileCal cells: Cell A5, a small one in sampling 12 (A) and cell D6, one of the largest cells in sampling 20 (B). The bias in η is clearly bigger for the larger cell.

5.2.1 Distance Correction

There is no spatial information of the muon track directly measured in the TileCal cell. Therefore the distance between the IP and the point of the measurement in the cell is calculated as if the muon would have travelled directly through the cell's centre. That leads to an inaccurate distance information, resulting in a mismeasurement of t_0.
That misinformation leads to a biased t_0 distribution as a function of η. As shown in Figure 5.2, this effect is much more significant for larger cells, than it is for smaller ones. Therefore the dependencies for the geometrical correction and calibration steps will be shown for one of the largest cells of the TileCal, cell D6.
The t_0 measurement is clearly biased for muons, which traverse the cell further apart from its centre. For muons in simulation (Figure 5.3b) the dependency on the η value of the track is even more significant than for muons in data (Figure 5.3a).

To correct for this bias, an algorithm adopted from [37], is implemented to calculate the real length of the path inside the cell.
Starting from the particle's ID information, the track is extrapolated to the corresponding TileCal cell. If the position of the production vertex differs from the IP, it was taken as origin of the track. From the spatial informations of the respective cell, the entry and exit points of the particle are calculated and the distance between them is defined as I_{track}. The centre of the line between these two points is then taken as the real position of the measurement. A sketch of the geometry of the distance correction is shown in Figure 5.4.

The distance between the tracks origin and the entry point of the track in the cell was used as d_{in}. The corrected new distance of the particles track is then computed as

$$d_{corr} = d_{in} + \frac{I_{track}}{2}. \tag{5.2}$$

As seen in Figure 3.7, the size of the different TileCal cells differs vastly. Therefore, for the large cells in sampling 20, the difference in the presumed particle path -

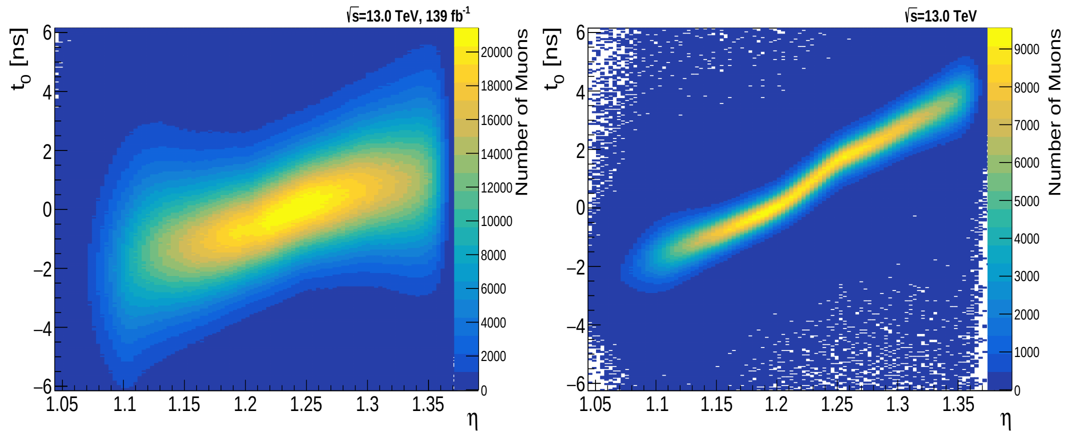

(A) (B)

FIGURE 5.3: The t_0 dependency on η before the distance correction i.e. for the uncorrected t_0 values. On the left for muons in data (A) and on the right for $Z \to \mu\mu$ muons in simulation (B). The plots both show the distribution in cell D6.

through the cell centre - and the real path can be up to 30 cm, as seen in Figure 5.5. To correct the t_0 measurement using d_{corr}, the additional ToF is substracted or added, depending on the sign of the difference, assuming the particle travelled that distance with the speed of light. The corrected t_0 is therefore calculated as

$$t_{0_{corr}} = t_0 + \frac{d_0 - d_{corr}}{c}. \tag{5.3}$$

As can be seen in Figure 5.6, the bias has been slightly removed, but especially for muons in simulation (Figure 5.6b) the dependency is still very present.
However, the overall t_0 measurement has clearly been improved by this procedure. Figure 5.7 and Figure 5.8 show the distribution of all t_0 values before and after the distance correction for muons in data and simulation, respectively.
The practical goal of all the correction and calibration steps is to improve the timing resolution, hence decrease the σ_{t_0} of the t_0 distribution, and shift its mean value as close to 0 ns as possible. The distance correction improves the σ_{t_0} by 48 ps (3%) for muons in data and by 13 ps (1.8%) for muons in simulation. The mean of the distribution has not been shifted by much. For simulation, the mean was even shifted further away from the expected value of 0 ns. To account for that, the residual bias is calibrated with the η-calibration.

5.2.2 η-calibration

The second step of the calibration is aiming at the same bias as the distance correction: the dependency of t_0 on the η value of the particle's track. But as the distance was corrected, we have to adjust for the fact that we don't know the actual velocity with which the particle is travelling that additional stretch. As this calibration is done for a search for HCLLPs, which are expected to travel with a velocity significantly smaller than the speed of light, this additional bias has to be accounted for. Because the slower the particles, the bigger the bias in η would be.

The calibration is done separately for data and simulation and follows a three-step

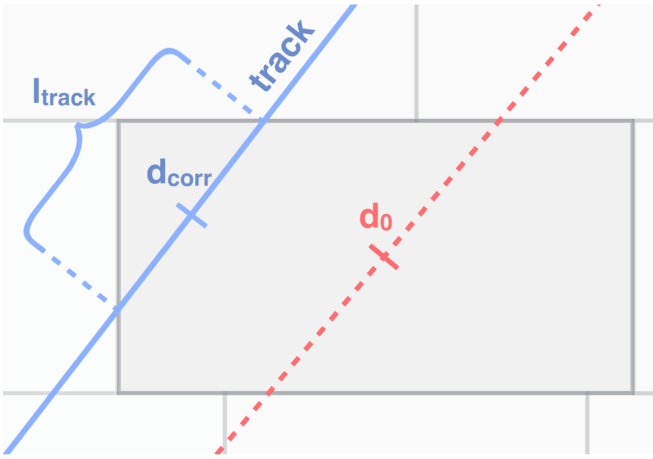

FIGURE 5.4: A schematic figure of a TileCal cell and the important properties for the distance correction. The blue line indicates the actual particle track and the red line the assumed track through the centre of the cell. d_0 marks the centre of the cell, while d_{corr} marks the actual point of the measurement. The length of the particles track is denoted as I_{track}. Figure taken from [26].

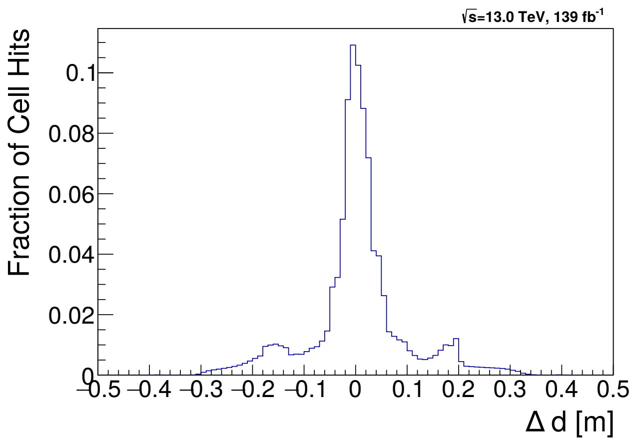

FIGURE 5.5: The distribution of the mismeasurement of the travelled distance. While the majority of the measurements are not to far apart from being correct, especially for the largest TileCal cells the miss-measurement can be up to 30 cm.

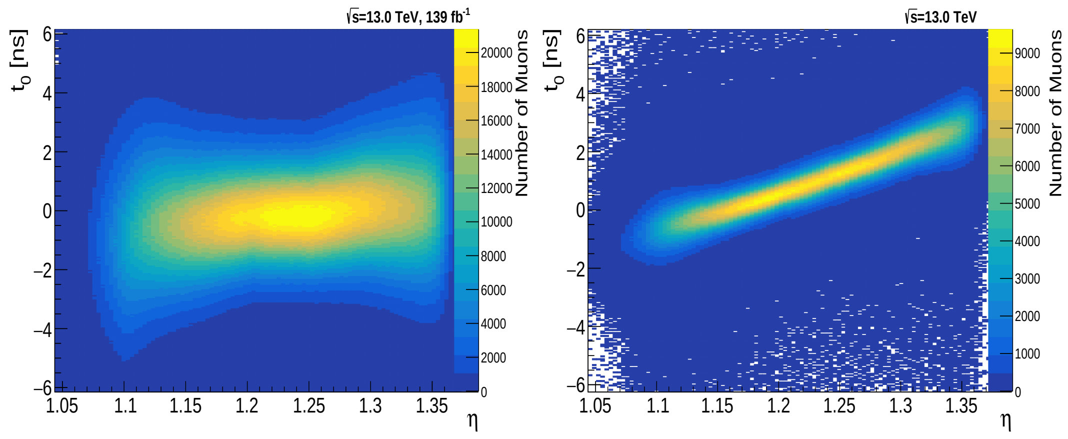

(A) (B)

FIGURE 5.6: The t_0 dependency on η after the distance correction for cell D6. On the left for muons in data (A) and on the right for $Z \to \mu\mu$ muons in simulation (B). The bias has been slightly corrected, but there is still some leftover bias present, especially for simulated events.

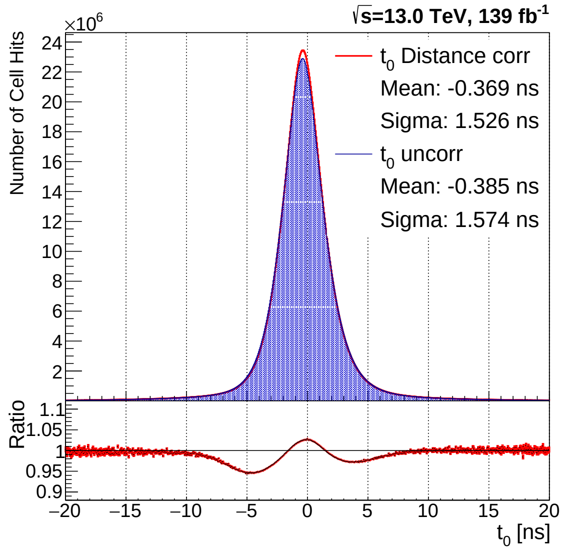

FIGURE 5.7: The t_0 distribution for all cells in the TileCal before and after the distance correction for muons in data. The correction clearly improved the σ_{t_0} of the distribution, thus improving the overall timing resolution.

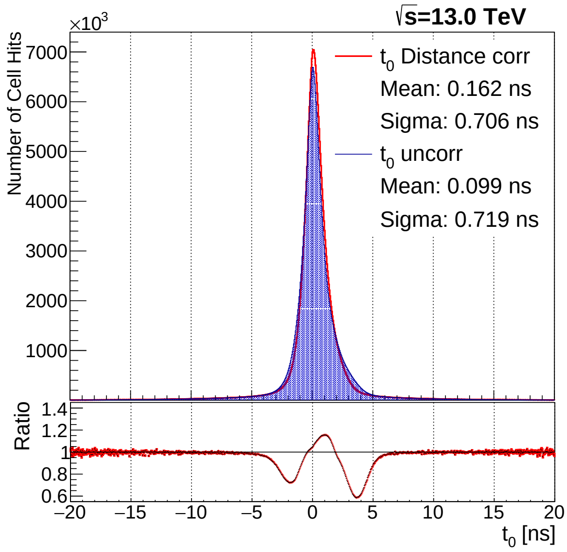

FIGURE 5.8: The t_0 distribution for all cells in the TileCal before and after the distance correction for muons in simulation.

procedure: For each of the 73 ϕ-projected cells, the t_0 distribution is plotted as a function of η (see Figure 5.6). That distribution is then split into several bins for different values of η. Depending on the size of the cell, the amount of η-bins ranges from 30 (for Cell C10) up to 97 (for Cell D6). The t_0 distribution of each slice is then fit with a Gaussian, using the range from the mean minus the **R**oot **M**ean **S**quare (**RMS**) to the mean plus the RMS. Subsequent to that, the distribution is fit with a Gaussian for a second time, using the mean of the first fit plus/minus the standard deviation σ of the first fit as range. The mean of the second Gaussian fit is then set as the calibration parameter for that η-bin of the corresponding TileCal cell. The distribution of the calibration parameters for cell D6 can be seen in Figure 5.9a. One example of a Gaussian fit to the t_0 distribution for one particular η-bin can be seen in Figure 5.9b. The ToF measurement is then calibrated by subtracting the corresponding calibration parameter from each t_0 value:

$$t_{0_{corr}} = t_0 - t_{mean} \tag{5.4}$$

After the η-calibration, the bias has been completely removed, as shown in Figure 5.10. The calibration effect can be seen in Figures 5.11 and 5.12, respectively. The distance correction effected the timing resolution σ_{t_0}, but left the mean of the distribution rather uncorrected. The η-calibration, on the other hand, caused an improvement of the mean by shifting it to almost 0 ns for both data (-0.003 ns) and simulation (-0.005 ns).
The σ_{t_0} of both distributions was also improved by 25 ps (1.6%) for muons in data and by 177 ps (25%) for muons in simulation. From the big effect of this calibration step, especially on simulated muons, it can be seen that the η dependence of the TileCal timing was vastly mis-modelled by the simulation.

Both η-dependent steps together improve the timing resolution by 4.6% in data and by 26.4% in simulation. A different approach to the η calibration is presented in Appendix A.3.

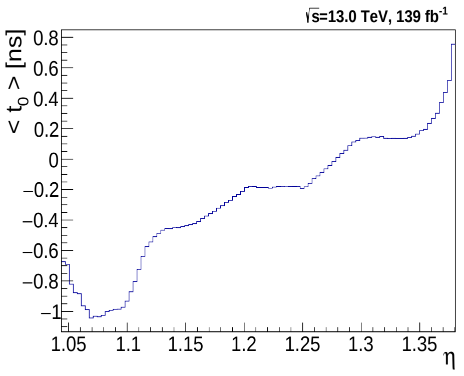

(A)

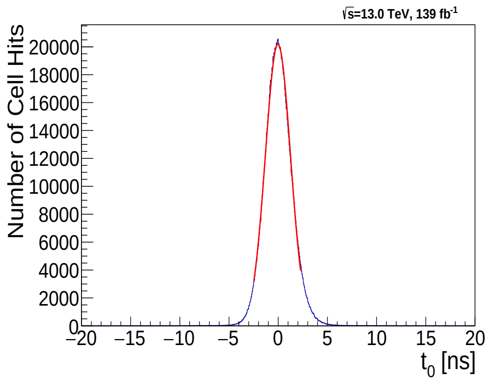

(B)

FIGURE 5.9: The calibration parameters for the η - calibration for cell D6 are shown in (A). (B) shows the slice for $1.2131 < \eta < 1.2168$ of cell D6 with the second Gaussian fit. The mean of the fit is used as the calibration parameter.

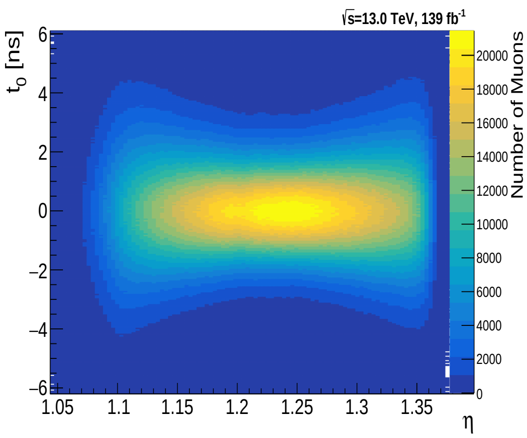

(A)

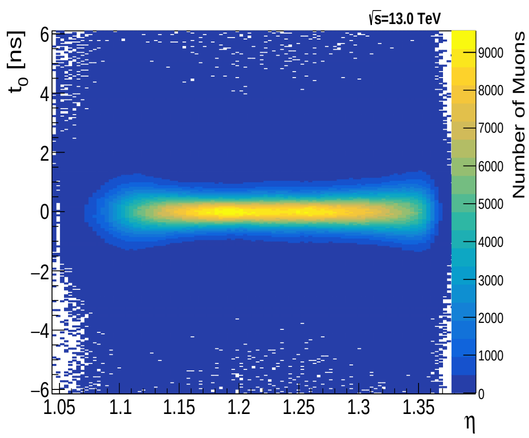

(B)

FIGURE 5.10: The dependency of the t_0 measurement on η after the η-calibration. (A) shows the calibrated dependency for muons in data and (B) for simulation. The bias has clearly been removed, both for data and simulation.

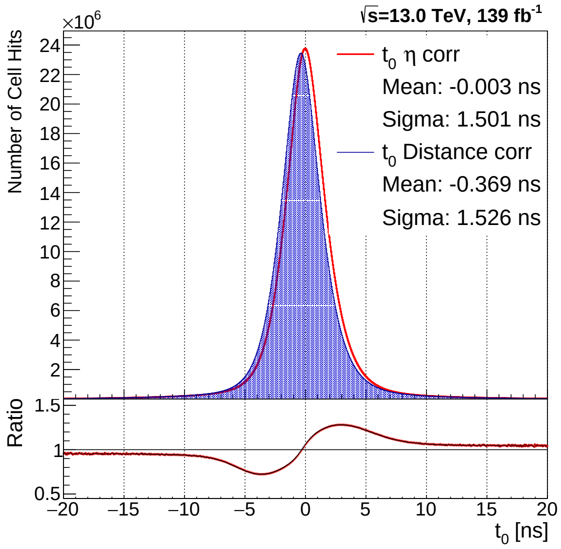

FIGURE 5.11: The t_0 distribution for all cells in the TileCal before and after the η-calibration for muons in data. Especially the mean of the distribution has been shifted closer to the expected value of 0 ns.

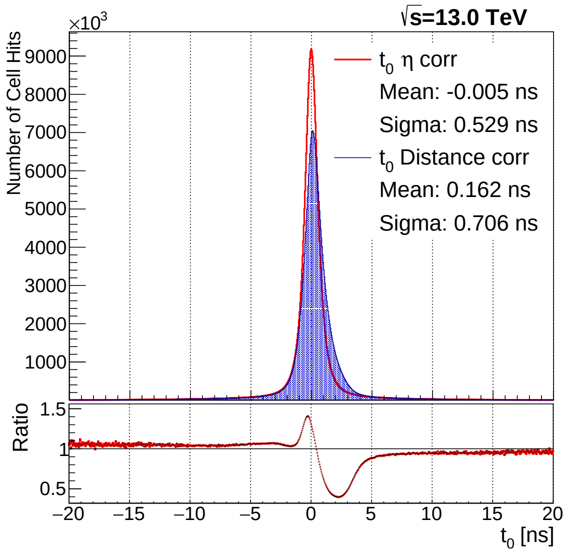

FIGURE 5.12: The t_0 distribution for all cells in the TileCal before and after the η-calibration for muons in simulation. The timing resolution is vastly improved by the η-calibration for simulation. Also the mean has been shifted almost completely to the expected value of 0 ns.

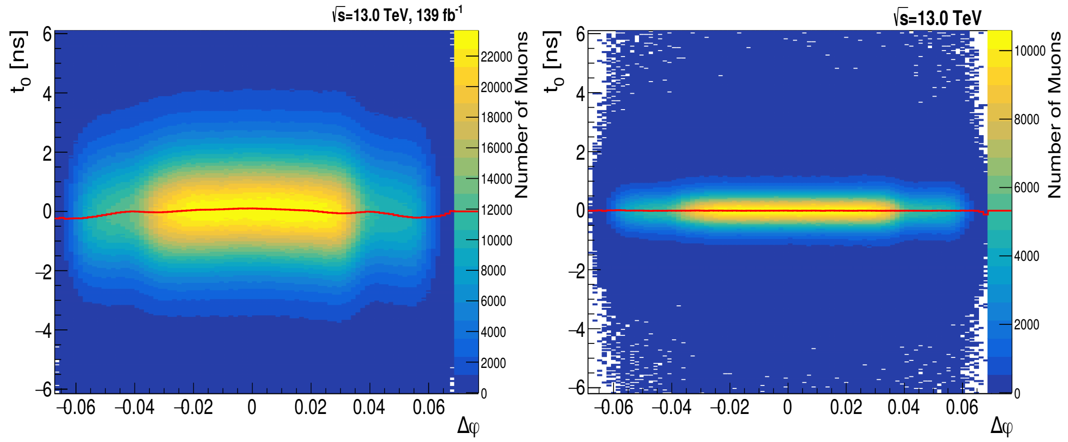

(A) (B)

FIGURE 5.13: The dependency of the t_0 measurement on $\Delta\phi$ before the ϕ-calibration. (A) shows the dependency for muons in data and (B) for simulation. The red lines show the superimposed profile of the t_0 mean values, which are used as calibration parameters.

5.2.3 ϕ-calibration

For the ϕ-calibration, no big effect on the overall timing resolution is expected. As explained before, all cells with the same geometrical properties have been combined to ϕ-projected cells, as we expect the timing measurement to be unbiased in its ϕ dependence. Nonetheless, with this calibration step, we confirm the symmetry in ϕ and calibrate for any possible leftover geometrical bias. As calibration variable, not the tracks ϕ value ϕ_{track} is used, but $\Delta\phi$, the difference between the ϕ value of the cell's centre ϕ_{cell} and ϕ_{track}:

$$\Delta\phi = \phi_{cell} - \phi_{track} \tag{5.5}$$

The dependency of the t_0 measurement on $\Delta\phi$ can be seen in Figure 5.13. As expected, the t_0 values are spread evenly around 0 ns with almost no bias visible for data (Figure 5.13a), as well as for simulation (Figure 5.13b). The mean t_0 values are constantly almost 0. However, for large absolute values of $\Delta\phi$, the means of the respective t_0 distributions are slightly below 0 ns. This leftover bias is accounted for by the ϕ calibration.

The calibration process is similar to the one of the η-calibration: The t_0 distribution is fit two times with a Gaussian, with the first fit being used to calculate the range parameters for the second one. The results of the ϕ-calibration can be seen in Figures 5.14 and 5.15. For muons in data, the timing resolution improves by 2 ps, while the mean also only changes insignificantly. For simulation even less is changed, as the resolution stays the same and the mean is changed by only 1 ps.

5.2.4 Energy Calibration

The energy calibration is applied to calibrate the bias of the ToF measurement depending on the amount of the deposited energy E_{Hit} in each corresponding TileCal cell. It can be seen in Figure 5.16, that the dependency of the timing measurement on the energy is larger for lower deposited energies E_{Hit}. The mean of the t_0 distribution

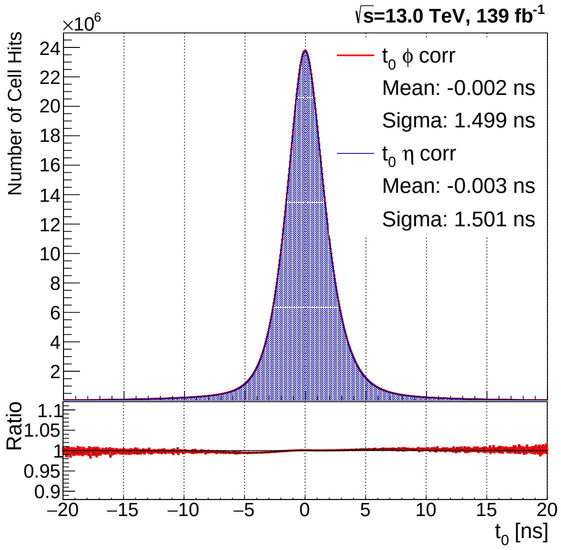

FIGURE 5.14: The t_0 distribution for all cells in the TileCal before and after the ϕ-calibration for muons in data. It is clear, that the ϕ-calibration doesn't improve the timing measurement much, thus confirming the expectation of an almost unbiased t_0 dependency on $\Delta\phi$.

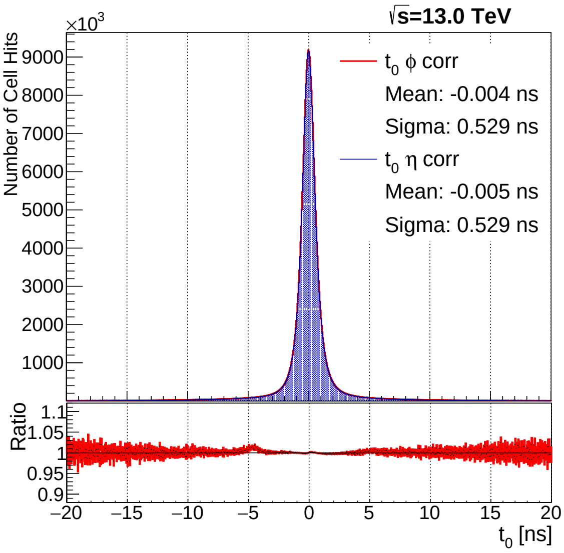

FIGURE 5.15: The t_0 distribution for all cells in the TileCal before and after the ϕ-calibration for muons in simulation.

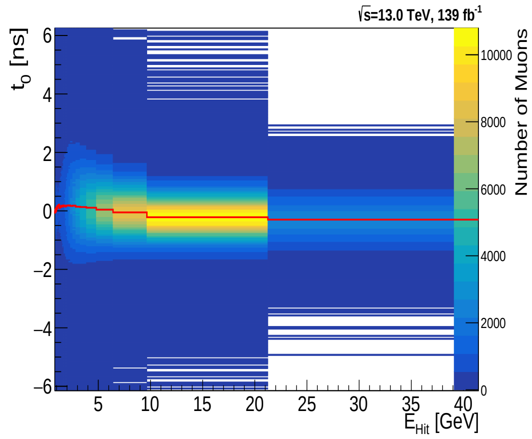

(A)

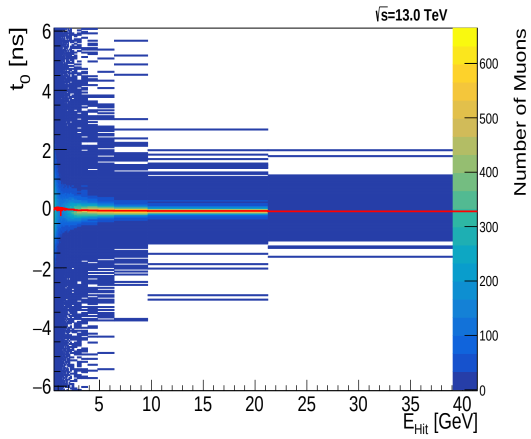

(B)

FIGURE 5.16: The dependency of the t_0 measurement on the deposited energy E_{Hit} before the energy calibration. (A) shows the dependency for muons in data and (B) for simulation. The red lines show the mean values of the single bin t_0 distributions, which are used as calibration parameters.

shows a clear deviation from 0 ns for low E_{Hit} values. Therefore a energy-dependent calibration is applied.

The energy calibration is done similarly to the two preceding calibration steps and for ϕ-projected cells. In contrast to the η- and ϕ-calibrations however, the binning was not chosen to be constant. As there are a lot more cell hits with a low E_{Hit} than there are with large energy deposits, the binning was chosen to have roughly the same statistics in each energy bin. Testing different bin distributions and total number of bins have shown that a number of 100 bins, all with about the same statistics, yield the best calibration results. More on these tests can be found in the Appendix A.2.

The results of the energy calibration for muons in data can be seen in Figure 5.17 and for muons in simulation in Figure 5.18. The timing resolution in data was improved by 6 ps (0.4%), while for simulation, the calibration only yielded an improvement by 1 ps (0.19%). The mean of the t_0 distribution for data has not been improved. In simulation however, the mean was shifted to the expected 0 ns.

5.2.5 Cell-wise Calibration

The cell-wise calibration is done separately for all 4672 single TileCal cells. A different approach for that step is shown in Appendix A.4. The calibration accounts for de-synchronisations of single TileCal cells. It is only applied for muons in data, as these kind of effects are not modelled in simulation. For this step, the t_0 distribution for each single cell is fitted with a Gaussian in the range mean plus/minus RMS. The mean of this fit is then used as the calibration parameter. The reason, why the calculation of the calibration parameters for the cell-wise calibration is slightly different then that of the first three steps, is the comparability with earlier studies regarding the timing measurement [26]. The results of the last analysis will be presented and compared to the current results in Chapter 6. Furthermore, a second Gaussian fit

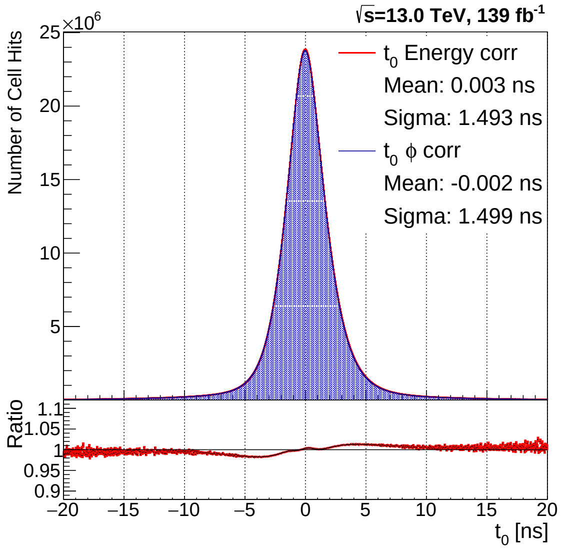

FIGURE 5.17: The t_0 distribution for all cells in the TileCal before and after the energy calibration for muons in data.

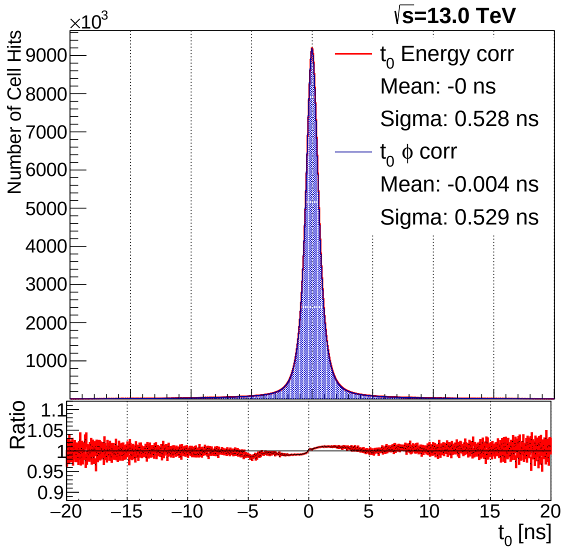

FIGURE 5.18: The t_0 distribution for all cells in the TileCal before and after the energy calibration for muons in simulation.

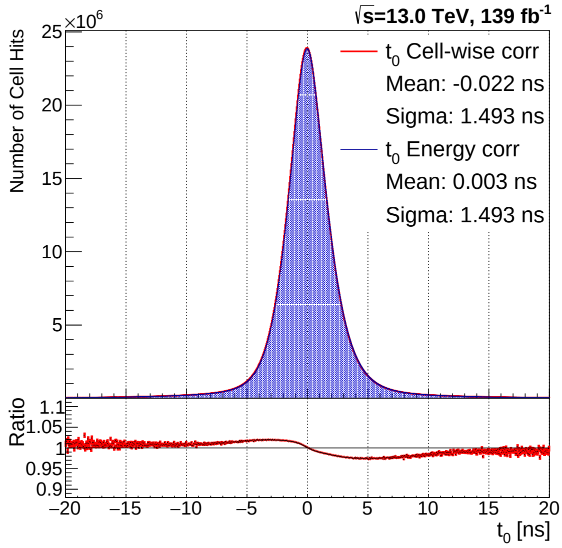

FIGURE 5.19: The t_0 distribution for all cells in the TileCal before and after the cell-wise calibration for muons in data.

would not change the observed results for this particular calibration step.
The calibrated t_0 for the cell-wise calibration is computed analogously to the three calibration steps prior. For almost every single cell, the absolute value of the mean of its specific t_0 distribution is below 230 ps. Therefore the effect of this calibration step is rather small, as the timing resolution has not been affected by it. The mean is even shifted a bit in the wrong direction, which can be seen in Figure 5.19. But nonetheless it is important to apply the cell-wise calibration, as it accounts for cells with systematic mismeasurements.

5.2.6 Run-wise Calibration

The timing measurement shows a dependency on the specific run of its data-taking. The discrepancy between the expected and the measured mean t_0 values can be explained by a desynchronisation between the LHC clock and the actual time of the collision. These desynchronisations can originate from weather influences on the signal transmitting fibres used in the ATLAS detector [26]. As can be seen in Figure 5.20, the mean values of the run-wise t_0 distributions are rather stable for most of the data. Especially for the 2017 and 2018 data, only fluctuations of about 0.15 ns are observed. For the beginning of Run–2 in 2015 however, there have been fluctuations of up to 0.4 ns. The improvement of the fluctuations over the years can be explained by an improvement of the online monitoring of the timing.
The effect of the run-wise calibration step on the overall timing resolution can be seen in Figure 5.21. The resolution has been improved marginally by 2 ps, whereas the mean of the t_0 distribution has not changed at all. That was expected, as the majority of the data used for this calibration originates from 2017 and 2018, where the timing was quite stable. Although the effect is not huge, the run-wise calibration is nonetheless important, as it assures a stable timing measurement over the full four years of data-taking during Run–2.

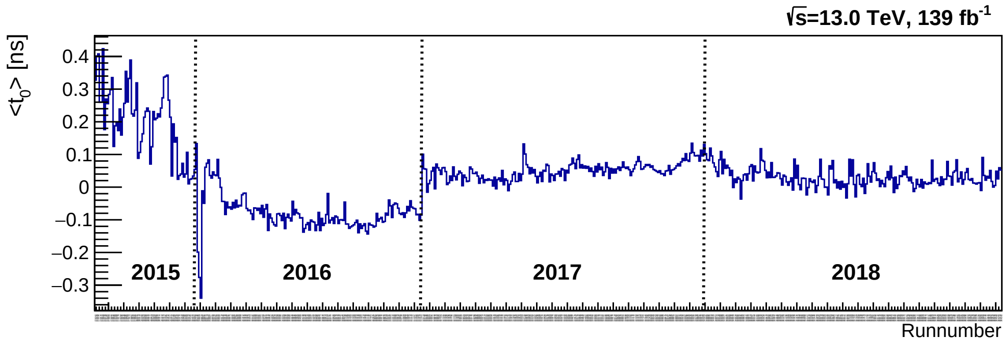

FIGURE 5.20: The mean t_0 distribution for all used Runnumbers for muons in data. The dotted lines show the separate years of data taking.

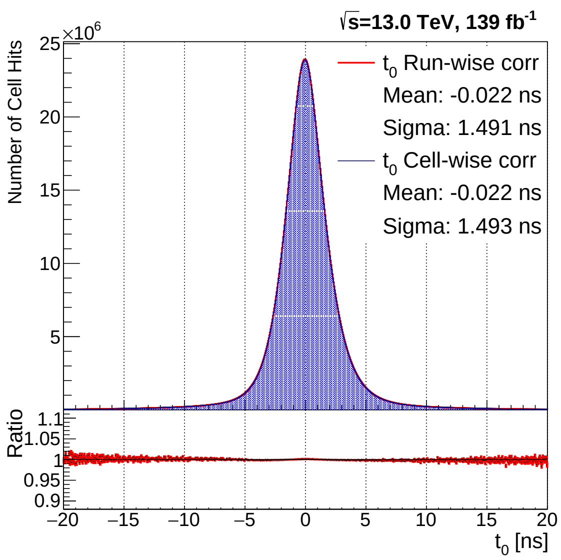

FIGURE 5.21: The t_0 distribution for all cells in the TileCal before and after the run-wise calibration for muons in data.

5.2.7 Smearing

The timing resolution in simulated $Z \rightarrow \mu\mu$ events is quite different than that in data, as can be understood by comparing the final timing resolutions in data (σ_{t_0} = 1.491 ns (see Figure 5.21)) and simulation (σ_{t_0} = 0.528 ns (see Figure 5.18)). Therefore, a smearing is applied to the simulated t_0 distribution. The smearing is chosen to be energy-dependent, as the dependency of the timing resolution on the deposited E_{Hit} per cell differs for some of the TileCal cells, especially the larger ones. That dependency is shown in Figures 5.22a and 5.22b for the rather small cell A10 and in Figures 5.22c and 5.22d for one of the largest cells, D5. These figures are produced quite similarly to the calibration parameters of the energy calibration step, but instead of using the mean of the t_0 distribution per E_{Hit}-bin, now the standard deviation σ of the second Gaussian fit of the distribution is drawn.
Due to the lower statistics for higher energy deposits E_{Hit}, the resolution is calculated separately for high-gain (E_{Hit} < 20 GeV) and low-gain (E_{Hit} > 20 GeV) signals. For low-gain signals only one bin is used, as the amount of cell hits with that energy deposit is rather low.
To further increase the statistics for this calculation, both sides of the detector are combined. The difference in the σ_{t_0}-distributions is mostly caused by the geometric shape of the different cells, therefore we can combine the measurements of e.g. Cell A10 and Cell -A10 to increase the statistics for the different distributions. Thus, for the smearing step, if e.g. cell A10 is mentioned, it refers to the combination of cells A10 and -A10. A comparison between the results achieved as explained above and the results achieved without combining both sides of the detector can be found in Appendix A.5.

It is clearly visible, that the σ_{t_0} distribution is different for data and simulation. For cell A10, only for high energies does the distribution show a difference, as the curve is suddenly rising for hits with an E_{Hit} of 20 GeV or higher. For the larger cell D5 though, there is a clear unphysical rise in the simulated σ_{t_0} distribution.
This rise is corrected by applying the smearing to the simulated events. The energy-dependent timing resolution $\sigma_{t_0}(E_{Hit}, \text{cell})$ is parametrised for the high-gain measurements in data using this three-parameter function:

$$\sigma_{t_{0_{data}}} = \sqrt{p_0^2 + (p_1^2/\sqrt{E})^2 + (p_2^2/E)^2} \tag{5.6}$$

This equation consists of three different terms, one constant term, one statistical term depending on $\sqrt{E}$ and one noise term depending on E, where E is the individual deposited energy E_{Hit} per measurement. For simulation, this parametrisation has to be modified to account for the unphysical rise. Therefore a $\tan^{-1}$ term is added to Equation 5.6:

$$\sigma_{t_{0_{sim}}} = \sqrt{p_0^2 + (p_1^2/\sqrt{E})^2 + (p_2^2/E)^2} + \tan^{-1}(E + p_3)p_4 - p_5. \tag{5.7}$$

These parametrisations of σ_{t_0} are then used to smear the t_0 distribution in simulation. For that purpose the simulated t_0 values after the energy calibration are changed by a random-number smearing value. That smearing value is randomly chosen from a Gaussian with mean zero and the standard deviation defined as the difference in the σ_{t_0} values corresponding to the E_{Hit} and the cell of the individual measurement.

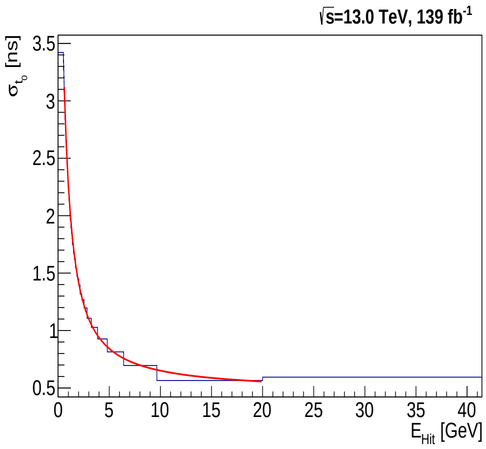

(A)

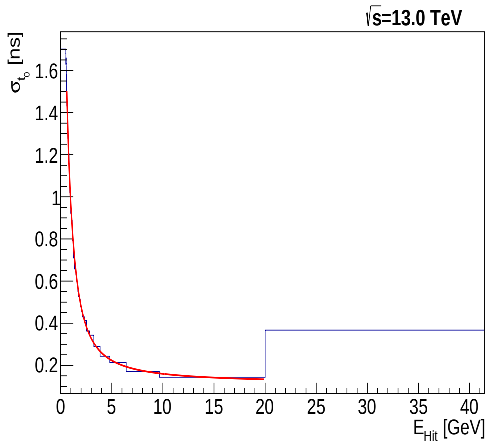

(B)

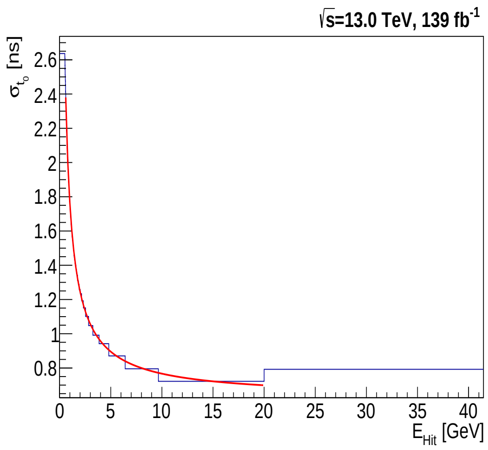

(C)

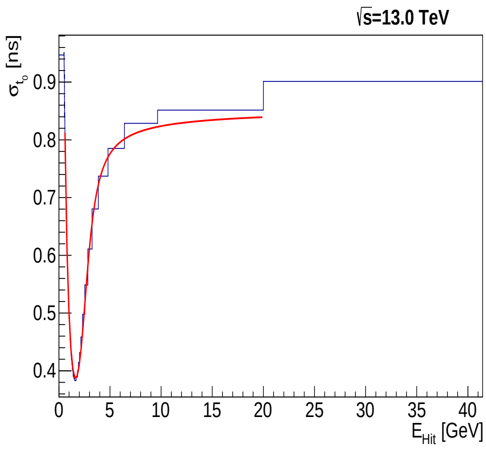

(D)

FIGURE 5.22: The dependency of the t_0 resolution on the deposited energy E_{Hit}. The upper row ((A)+(B)) shows the Plots for cell A10 and in the lower row ((C)+(D)) the plots for cell D5 are presented. The plots in the left column are for muons in data, whereas the right column shows the results for muons in simulation. For the simulated events, a clear rise of σ_{t_0} is observed. For the smaller cell A10, the rise is only small, whereas for the larger cell D5, the rise is significant and covers almost the whole σ_{t_0} range.

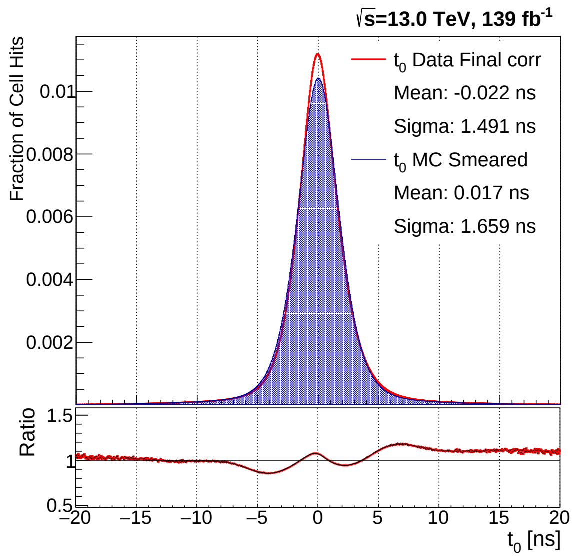

FIGURE 5.23: The final t_0 distribution for all cells in the TileCal for data and the smeared t_0 distribution for simulation.

$$t_{0_{smeared}} = t_0 + Random.Gaus\left(0, \sqrt{\sigma^2_{data}(E_{Hit}, cell) - \sigma^2_{sim}(E_{Hit}, cell)}\right). \tag{5.8}$$

For some really rare cases, the resolution in data is better than that for simulation, resulting in a problem for Equation 5.8. These cases are so rare, that sacking these measurements does not effect the statistics and the discrepancy is usually so small, that no correction was applied.

The final t_0 distributions for muons in data after all calibrations and for muons in simulation after the smearing can be found in Figure 5.23. The goal was to smear the t_0 distribution of simulated events in a way, that it shows exactly the same properties as its data counterpart. However, the smeared distribution shows a worse standard deviation than the one for data, implicating an overcorrection by the smearing process. That could hint to the need for a different parametrisation for the σ_{t_0} distribution or the existence of further discrepancies between the simulated and the actual timing measurement.

5.2.8 Pull Correction

To correct the final β measurement for asymmetries in the distribution, a pull correction is applied as the last step, separately for data and simulation. In the smearing step, an individual, per cell, energy-dependent uncertainty of the t_0-measurement was calculated both for data and simulation. For data, that same uncertainty σ_{t_0} (E_{Hit}, cell) is also used to calculate the uncertainty of the final β measurement in the TileCal. In the case of simulation, a new σ_{t_0} (E_{Hit}, cell) is computed analogously to the smearing step using the smeared t_0 values for the calculation of the uncertainty.
That t_0 uncertainty is now used to calculate the uncertainty of the inverse β measurement as:

$$\sigma_{\beta^{-1}} = \frac{c \cdot \sigma_{t_0}(E_{Hit}, cell)}{d} \tag{5.9}$$

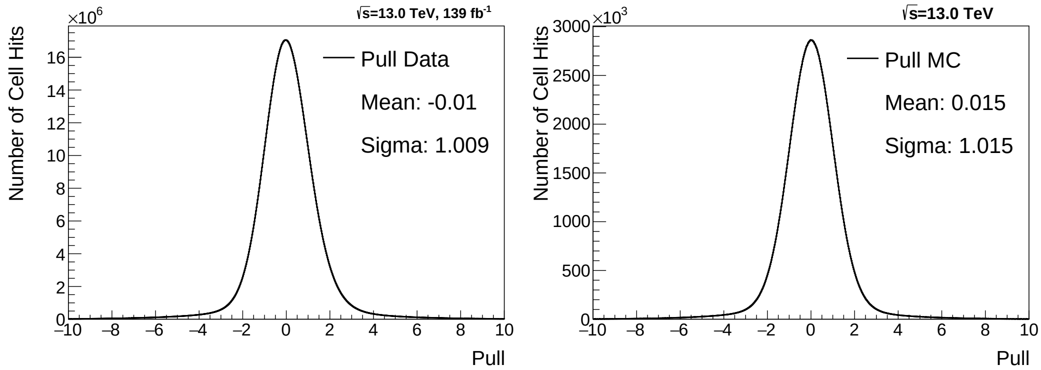

(A) (B)

FIGURE 5.24: The pull distribution for data (A) and for simulation (B). The discrepancy from a unit Gaussian for data is only 0.9%, for simulation it is 1.5%.

With this inverse β uncertainty, the pull is calculated as:

$$pull = \frac{\frac{1}{\beta_{reco}} - \frac{1}{\beta_{true}}}{\sigma_{\beta^{-1}}} \tag{5.10}$$

As the muons used in this calibration are all expected to travel with the speed of light in reference to the timing resolution of the TileCal, β_{true} equals 1 for the pull correction.
In the case of a perfect t_0 and β measurement, the pull distribution would just be a unit Gaussian with a mean at 0 and a standard deviation of 1.
The final pull distributions can be found in Figure 5.24. Both distributions are very close to a unit Gaussian, with small discrepancies. For data, the pull distribution is almost perfect, with the standard deviation only differing from 1 by 0.9%. For simulation, the width of the distribution is off by 1.5%. Both values are improvements compared to the 1.6% (data) and 5% (simulation) deviations achieved in the previous analysis [26].
The resulting deviations of 0.9% and 1.5% are taken as constant scaling of the uncertainty.

5.3 Satellite–Satellite Collisions

The timing measurement of the ATLAS Tile calorimeter was calibrated to achieve the best possible timing resolution by using muons. For this calibration, we expected the muons to travel through the detector with $\beta = 1$. But in an analysis for the search for HCLLPs, those exact particles would not travel with, or almost with the speed of light. They would traverse the detector with a much lower velocity. Therefore the signals measured in the TileCal would be vastly out-of-time compared to that of SM particles.

To assure that the timing measurement with the TileCal is still usable for out-of-time signals, a method using muons from earlier or later collisions to check the timing resolution has been applied.

The LHC is filled with the main proton bunches every 25 ns, but due to the 400 MHz RF System, there exist possible bunch fillings every 2.5 ns. The Super Proton

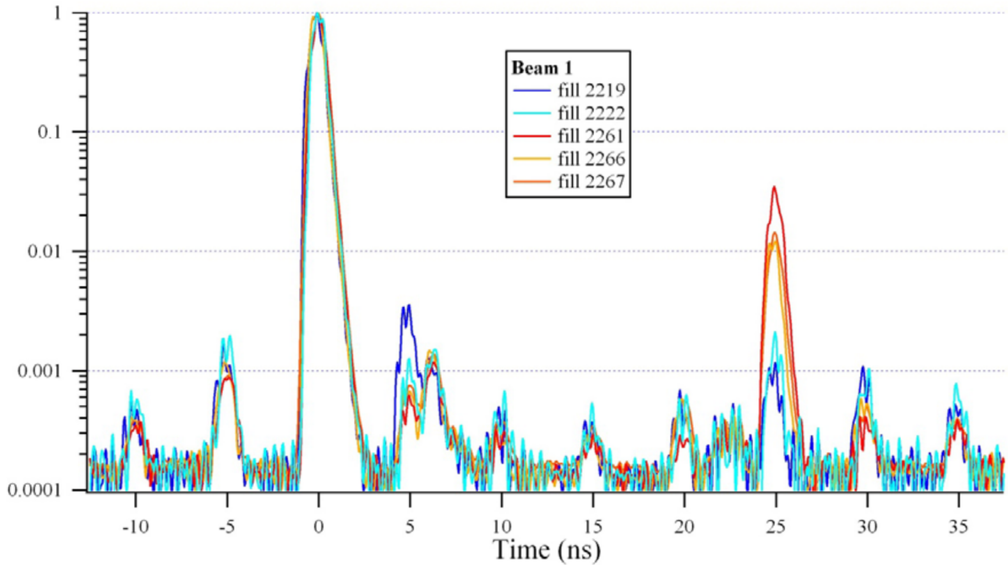

FIGURE 5.25: The LHC bunch population for some proton-proton fills. Longitudinal profile of the filled slot and the following slots, showing the effect of satellite enhancement in the LHC injector chain. The fills 2219 and 2222 used the normal bunch splitting scheme, whereas fills 2261, 2266 and 2267 used the modified scheme with enhance satellites. This figure and the explanation was taken from [38].

Synchroton, the last pre-accelerator before the injection into the LHC, is driven by a 200 MHz system, meaning that only every 5 ns a bunch is filled significantly [39]. In Figure 5.25 it can be clearly seen that the side bunches at plus/minus 5 ns are the most populated. However, the population of these so-called satellite bunches is suppressed by a factor $\mathcal{O}(10^{-3})$. That leads to a suppression of the plus/minus 5 ns satellite–satellite collisions by $\mathcal{O}(10^{-6})$.

So the main difficulty is identifying the muons that originate from these satellite–satellite collisions. When identified, they can be used to validate the timing measurement of the TileCal for real out-of-time signals.
But as can be seen in Figure 5.26, the tails of the calibrated t_0 distribution are only suppressed by $\mathcal{O}(10^{-2})$, making it impossible to see any possible muons originating from satellite-satellite collisions.

To being able to possibly identify those muons from satellite–satellite collisions, a method taken from [26] has been applied. For the identification of satellite muons, the individual ToF measurement has been merged for muons with multiple cell hits to calculate a combined $t_{0_{combined}}$ per muon as

$$t_{0_{combined}} = \frac{\sum_{i=1}^{N} t_{0_i}/\sigma^2_{t_{0_i}}}{\sum_{i=1}^{N} 1/\sigma^2_{t_{0_i}}} \tag{5.11}$$

where t_{0_i} is the individual t_0 measurement and $\sigma_{t_{0_i}}$ the estimated uncertainty of the corresponding ϕ-projected TileCal cell. Furthermore, two other specific properties of potential satellite muons are calculated and used as discriminating variables: The combined uncertainty $\sigma^2_{t_{0_{comb}}}$, which is calculated as

$$\sigma^2_{t_{0_{comb}}} = \frac{1}{\sum_{i=1}^{N} 1/\sigma^2_{t_{0_i}}}, \tag{5.12}$$

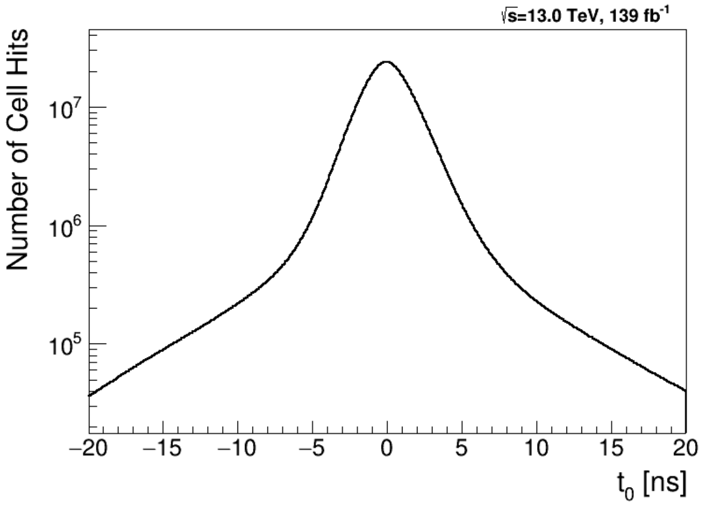

FIGURE 5.26: The t_0 distribution after all calibrations for muons in data with a logarithmic y-axis. The tails at plus/minus 5 ns are only suppressed by a little less than $\mathcal{O}(10^{-2})$, completely covering all traces of muons originating from satellite-satellite collisions which are assumed to be suppressed by $\mathcal{O}(10^{-6})$.

and the consistency χ^2. The consistency estimates a measure of the discrepancy between the individual t_0 measurements and the combined $t_{0_{combined}}$. It is calculated as

$$\chi^2 = \sum_{i=1}^{N} \frac{(t_{0_{combined}} - t_{0_i})^2}{\sigma^2_{t_{0_i}}}. \tag{5.13}$$

All possible muons in data are then evaluated by their respective $\sigma^2_{t_{0_{comb}}}$ and the probability P(χ^2, $N_{hits} - 1$) that all used cell hits are originating from the same muon. The 2D-plane of $\sigma^2_{t_{0_{comb}}}$ and P is first scanned to find the best pair of variables to suppress the tails of the t_0 distribution enough to resolve the side-peaks at plus/minus 5 ns. Unfortunately so far no combination of the two variables could sufficiently suppress the tails and leave enough statistics for the side-peaks being able to be fit with a Gaussian.
The combination with the visibly best reduction of the tails and the best left-over statistics for eventual side-peaks was found to be $\sigma^2_{t_{0_{comb}}} < 0.75$ ns and P(χ^2, $N_{hits} - 1$) > 0.7. The corresponding t_0 distribution can be seen in Figure 5.27.

5.4 Final t_0 and β Distributions

The correction and calibration steps described in this chapter significantly improved the timing resolution of the TileCal. The total improvement of the t_0 distribution for muons in data can be seen in Figure 5.28. The mean was shifted by 0.363 ns towards the ideal value of 0 ns. The timing resolution was improved by 83 ps, which is a relative improvement of 5.3%. Most of the improvement originated from the geometrical distance correction and η-calibration, but all steps are valuable for the guarantee of a stable timing measurement.

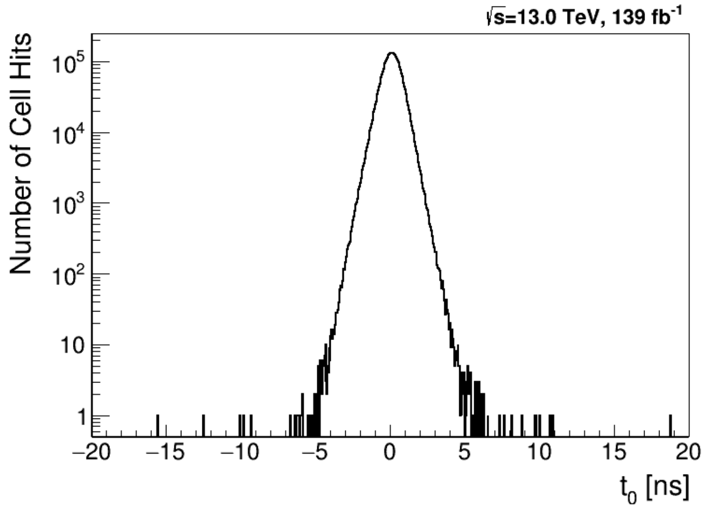

FIGURE 5.27: The t_0 distribution for the identification of possible satellite muons.

To achieve the best possible β measurement, not the individual β values calculated as

$$\beta_{corr} = \frac{d_{corr}}{t_{0_{corr}} \cdot c + d_0} \tag{5.14}$$

are used, but a weighted average combining all cell hits by a single particle. The inverse of the combined β_{Tile} is then calculated as

$$\beta_{Tile}^{-1} = \frac{\sum_{i=1}^{N} \beta_i^{-1} / \sigma^2_{\beta_i^{-1}}}{\sum_{i=1}^{N} 1/\sigma^2_{\beta_i^{-1}}}. \tag{5.15}$$

The inverse of β_{Tile} was used, because of its proportionality to t_0, making it easier to use the t_0 uncertainties σ_{t_0}. Therefore it is possible to compute an uncertainty for the combined β_{Tile} as

$$\sigma^2_{\beta^{-1}} = \frac{1}{\sum_{i=1}^{N} 1/\sigma^2_{\beta_i^{-1}}} \tag{5.16}$$

with this uncertainty of the inverse β being used to calculate the β uncertainty as

$$\sigma_\beta = \beta^2 \sigma_{\beta^{-1}}. \tag{5.17}$$

The final combined β_{Tile} distribution can be seen in Figure 5.29. The final resolution achieved is 0.076, which is a 10.5% deterioration from the resolution achieved in the previous analysis, which used 2015 and 2016 Run–2 data [40]. The reason for this degradation is probably the increase in pile-up, leading to a worsened β resolution. That difference in the β measurement for the different years of data-taking will be discussed in Chapter 6. A comparison between the calibration results for the timing measurement in this thesis and from the previous analysis can be found in Appendix A.1.

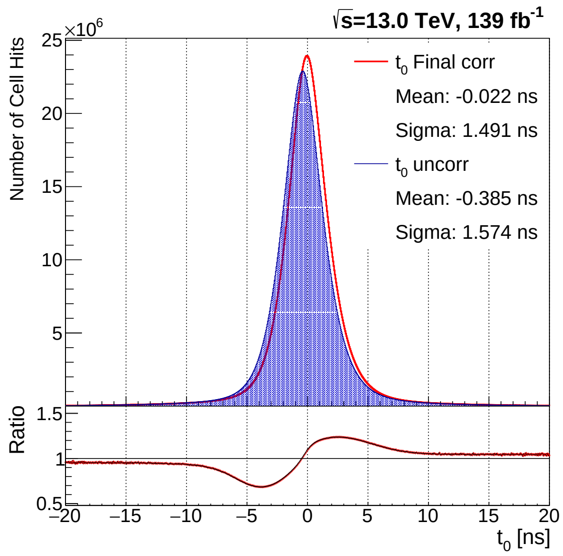

FIGURE 5.28: The t_0 distribution for all cells in the TileCal before and after all calibration steps for muons in data.

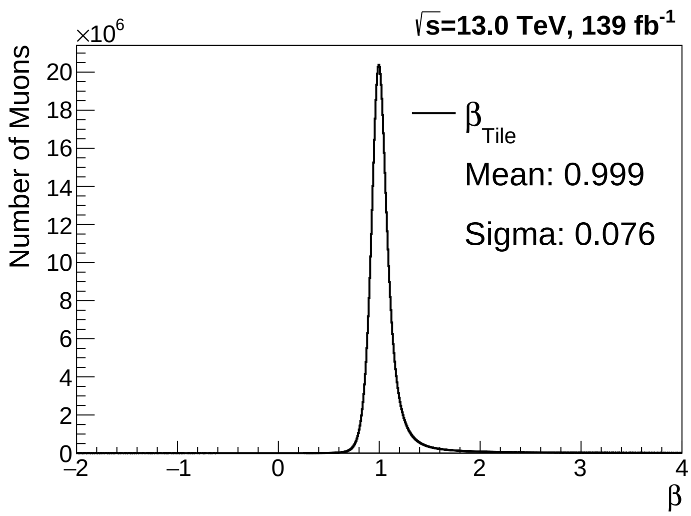

FIGURE 5.29: The final β distribution for all cells in the TileCal for muons in data.

Chapter 6

Studies on the timing measurement

In the previous chapter, all calibrations to achieve the best possible timing measurement with the ATLAS TileCal have been presented in their final version. All of the pre-requisites, calibration steps and parameters that have been used were shown. There are some studies on the timing measurement, however, that have been performed to either find the best parameters for the calibration, or to test, if the used version yields the best results.

The required minimum deposited energy per cell hit $E_{Hit_{min}}$ has been set to 500 MeV, but the effect of lower energy thresholds has been tested. It has been observed, that the timing resolution has changed over the years of data-taking in Run–2. These effects are presented in the following. Furthermore, the order of the correction and calibration steps has been presented in Section 5.2, but also a different order could be applied. The results of different correction orders is also presented in this chapter.

6.1 Energy threshold

One of the major cuts applied to select the cell hits used for the presented calibration is the minimum energy per cell hit $E_{Hit_{min}}$. For the results presented in Chapter 5 an $E_{Hit_{min}}$ of 500 MeV has been chosen. This energy threshold guaranteed the suppression of most of the detector noise, enabling a stable timing measurement. Furthermore it ensured a reasonable statistic for all calibration steps, even if further subdivisions have been applied, like the division in single TileCal cells for the cell-wise calibration step or the division in single η, ϕ or energy bins for these steps, respectively. But on the other hand, the dismissal of all cell hits with a deposited energy of less than 500 MeV leads to a decrease of muons with multiple cell hits. As shown in Figure 6.1, the fraction of muons with more than two cell hits is steadily decreasing with increasing energy thresholds. Whereas for an $E_{Hit_{min}}$ of 350 MeV the most probable number of cell hits for muons with at least one hit was three, for higher energy cuts the most probable amount of hits per muon has decreased to only two.

The obvious disadvantage of using a lower $E_{Hit_{min}}$ threshold is the decline of the overall timing resolution due to an increase of detector noise. As shown in Section 5.2.7, the t_0 measurement is dependent on the deposited energy, with an increased resolution for high-energy cell hits. As can be seen in Figure 6.2, the uncorrected t_0 distributions as well as the final corrected t_0 distributions show an increased overall timing resolution for higher $E_{Hit_{min}}$ thresholds. For $E_{Hit_{min}} > 350$ MeV the t_0 distribution after all calibrations has an uncertainty of 1.61 ns, whereas the 'standard' calibrated t_0 distribution for $E_{Hit_{min}} > 500$ MeV has an uncertainty of 1.491 ns. Also the relative improvement of the timing measurement is increasing

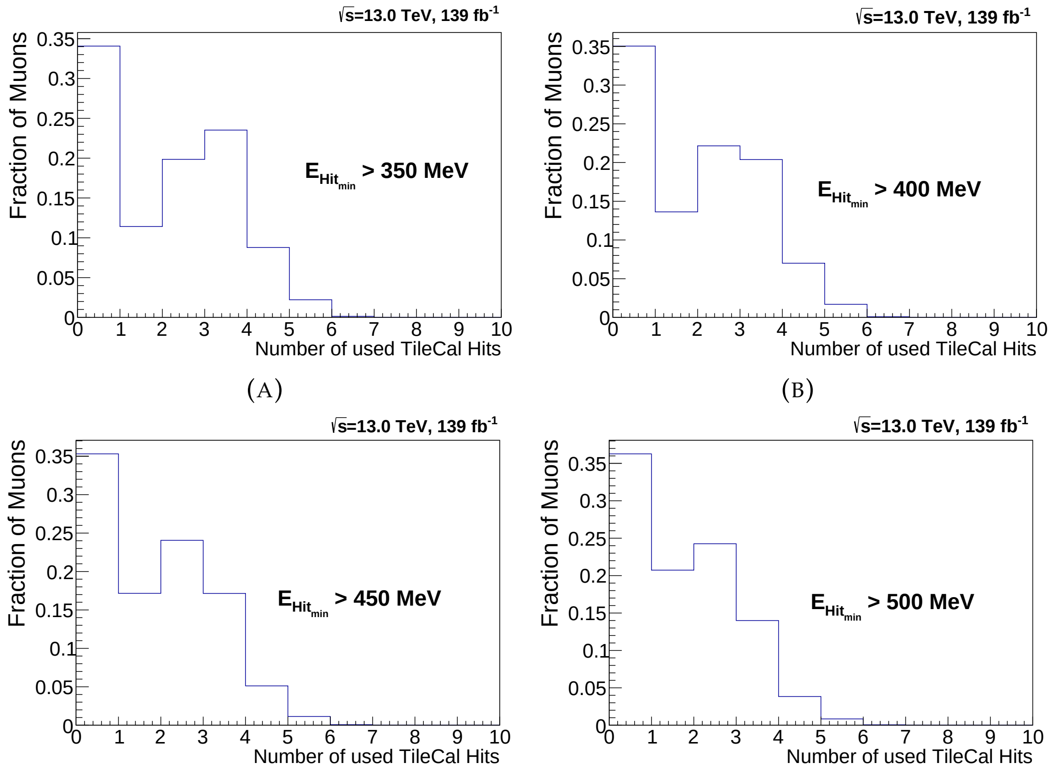

(A) (B) (C) (D)

FIGURE 6.1: Number of TileCal cell hits per muon for different $E_{Hit_{min}}$ thresholds. (A) shows the distribution for a cut of $E_{Hit_{min}}$ > 350 MeV, (B) for $E_{Hit_{min}}$ > 400 MeV, (C) for $E_{Hit_{min}}$ > 450 MeV and (D) for $E_{Hit_{min}}$ > 500 MeV. The average number of cell hits per muon strictly decreases from 1.715 for $E_{Hit_{min}}$ > 350 MeV to 1.31 for $E_{Hit_{min}}$ > 500 MeV.

with higher energy thresholds. The relative improvements by the calibrations are 4.9 %, 5.1 %, 5.2 % and 5.3 %, respectively.

The interesting question to investigate now, is how these two contrasting effects, worse timing resolution but more multiple hits, influence the final β resolution.
For the Final β_{Tile} calculation, it is quite beneficial to have multiple cell hits per muon, as the precision of the β measurement is increasing for muons with multiple hits (see Equation 5.15).

The final β_{Tile} distributions for each of the four different $E_{Hit_{min}}$ thresholds are shown in Figure 6.3. The uncertainty of the final distributions is increasing for decreasing energy thresholds. That leaves the 'standard' $E_{Hit_{min}}$-cut of 500 MeV as the most beneficial for the β measurement in the TileCal. It could be interesting to test the effect of even higher energy thresholds and their effect on the timing and β resolution, but that has not been done in this thesis.

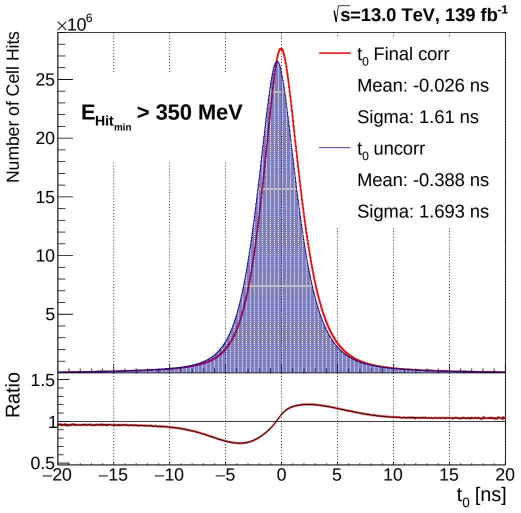

(A)

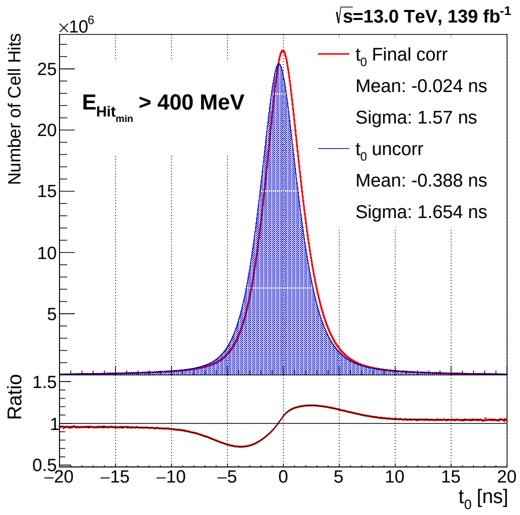

(B)

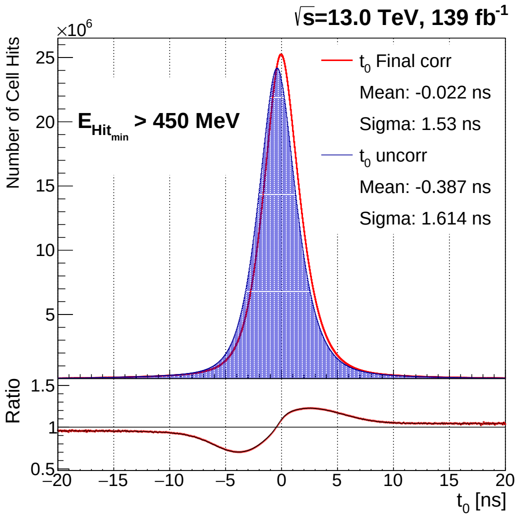

(C)

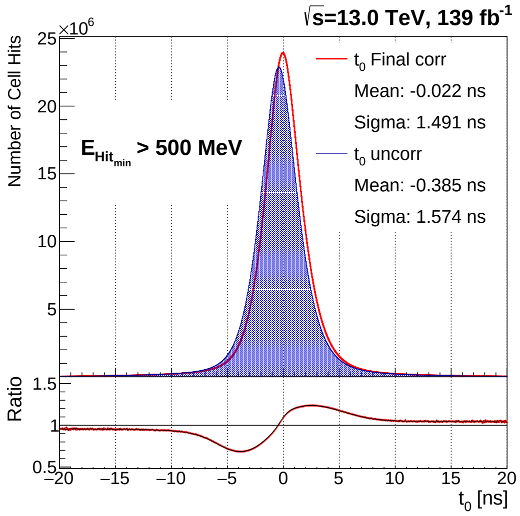

(D)

FIGURE 6.2: The t_0 distribution for all TileCal cells before and after all calibrations for muons in data. (A) shows the distribution for a cut of $E_{Hit_{min}}$ > 350 MeV, (B) for $E_{Hit_{min}}$ > 400 MeV, (C) for $E_{Hit_{min}}$ > 450 MeV and (D) for $E_{Hit_{min}}$ > 500 MeV. Both the uncorrected and the corrected distributions show a decreasing uncertainty for increasing energy thresholds as expected.

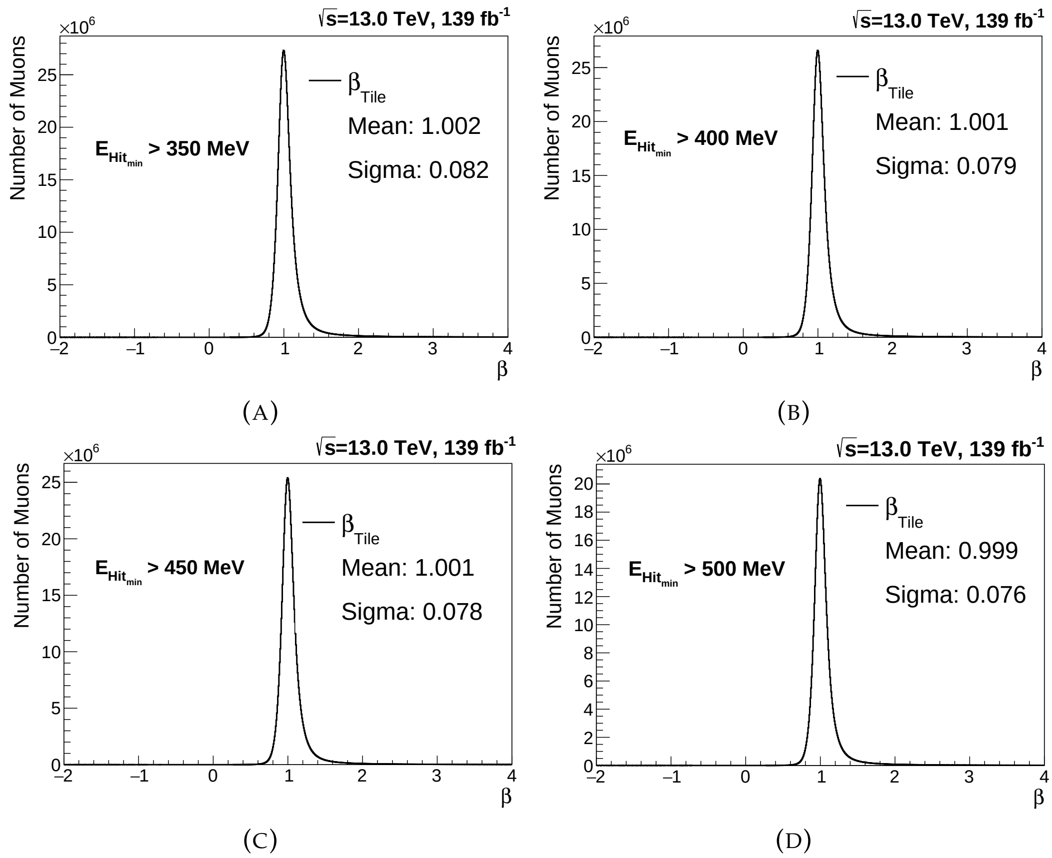

FIGURE 6.3: The β_{Tile} distribution for all qualifying muons in data before and after all calibrations. (A) shows the distribution for a cut of $E_{Hit_{min}} > 350$ MeV, (B) for $E_{Hit_{min}} > 400$ MeV, (C) for $E_{Hit_{min}} > 450$ MeV and (D) for $E_{Hit_{min}} > 500$ MeV. The uncertainty of the distributions is decreasing for higher energy thresholds.

6.2 Development of the timing resolution for different years of data-taking

As mentioned in Section 5.4, the final β_{Tile} resolution for the whole Run–2 data is worse than it was for the first 36.1 fb^{-1}. That leads to the question, how the resolutions of the timing and β measurements have developed over the four years of data-taking in Run–2.

In Figure 6.4 the uncorrected and final corrected t_0 distributions for each year of Run–2 are shown. It is clearly visible, that the uncertainties of the uncorrected, as well as those of the final corrected distributions have steadily increased over the four years of data-taking. The reason for that effect is probably the increase in pile-up over the years.

The overall development of the timing resolution can be seen in Figure 6.5. The uncertainty of the t_0 measurement is visibly increasing over the years with a major rise during 2016 and following that, a rather stable measurement. But nonetheless, also in 2017 and 2018 there is a small rise of the timing uncertainty. Furthermore, the rise is visible in both the uncorrected uncertainties (drawn in blue) and the final corrected uncertainties (drawn in red).

For the β measurement the uncertainties are shown in Figure 6.6. The blue line shows the uncorrected β_{Tile} uncertainties, the red line the final corrected ones.
An increase of the uncertainty is also visible for the β uncertainties, but interestingly, the final corrected uncertainties are rising much less, than the uncorrected ones. That effect could originate from the calibration implied by the run-wise step acting on the 2016 data, where a constant shift of the mean of timing measurement was observed (see Figure 5.20). However, that effect was not investigated further due to time restraints.

Another interesting question is, if the performance of the total calibration is impacted, whether only one set of calibration parameters is used for all of the Run–2 data, or whether specific sets for different time periods are calculated and used.

In the presented calibration in Chapter 5 only one set of calibration parameters was used. In a test of the aforementioned question, four different sets of calibration parameters, one for each year, have been calculated and applied specifically to their respective set of data. The result of the calibration with four different sets can be seen in Figure 6.7. The timing resolution has been slightly improved in comparison to the 'standard' calibrated distribution. That result was not yet used in Chapter 5 and Chapter 6, as all the different tests and studies could not have been re-done, using the method of multiple sets of calibration parameters, due to time restraints. So to ensure comparability, only one set of parameters was used for all results except Figure 6.7.

That result begs the question, if an even further splitting of the calibration parameters into periods or even single runs could further improve the effect of the calibration. However, a division into even smaller sets of data would lead to a drastic decrease of the usable statistics for the calculation of the calibration parameters. That would then be counterproductive towards the overall calibration efficiency. But nonetheless, it could be an interesting question to study in future analyses.

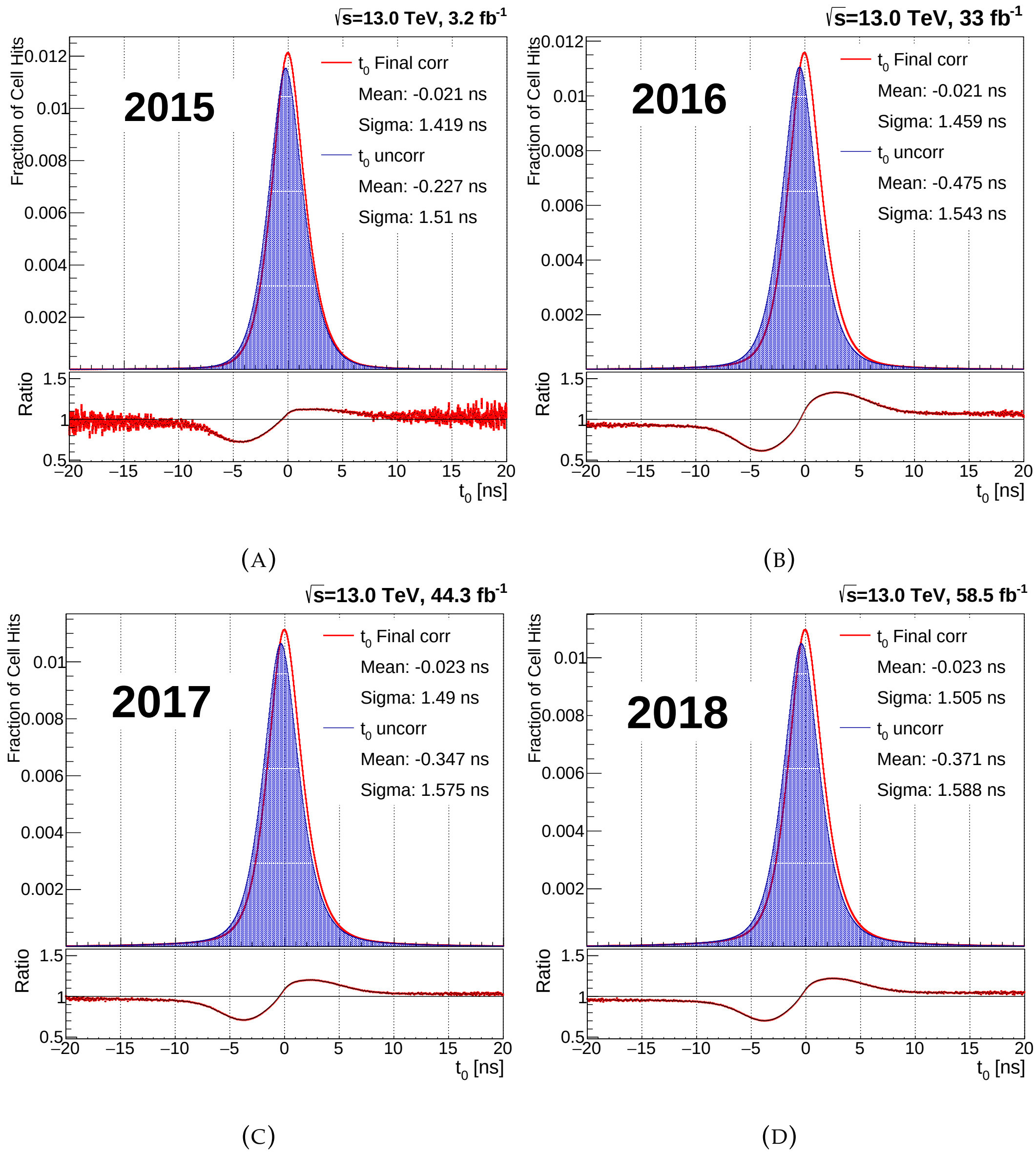

FIGURE 6.4: The t_0 distribution for all TileCal cells before and after all calibrations for muons in data. (A) shows the distribution for 2015 data, (B) for 2016 data, (C) for 2017 data and (D) for 2018 data. Both the uncorrected and the corrected distributions show an increasing uncertainty over the years from 2015 to 2018.

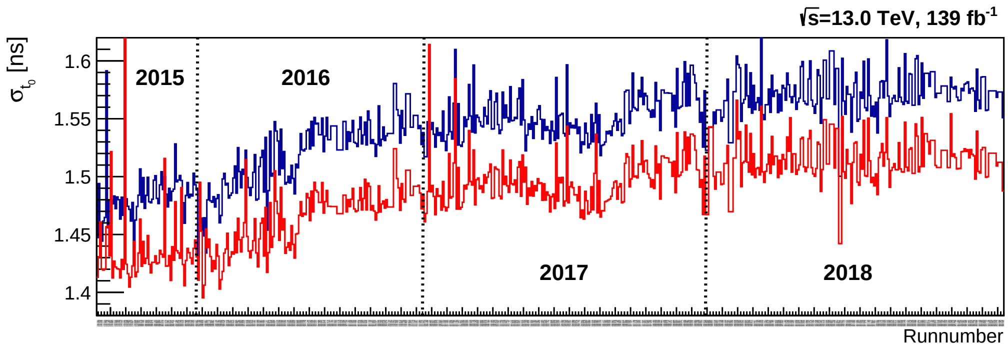

FIGURE 6.5: The timing uncertainties for all used Runnumbers for muons in data before and after all calibrations. The dotted lines show the separate years of data taking.

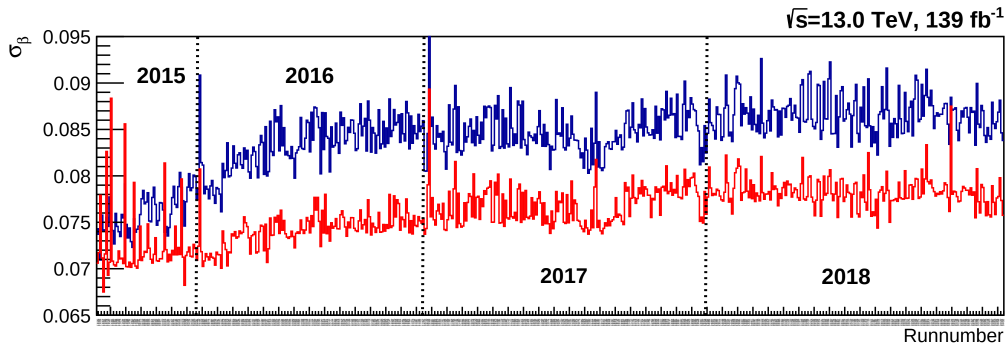

FIGURE 6.6: The β_{Tile} uncertainties for all used Runnumbers for muons in data before and after all calibrations. The dotted lines show the separate years of data taking.

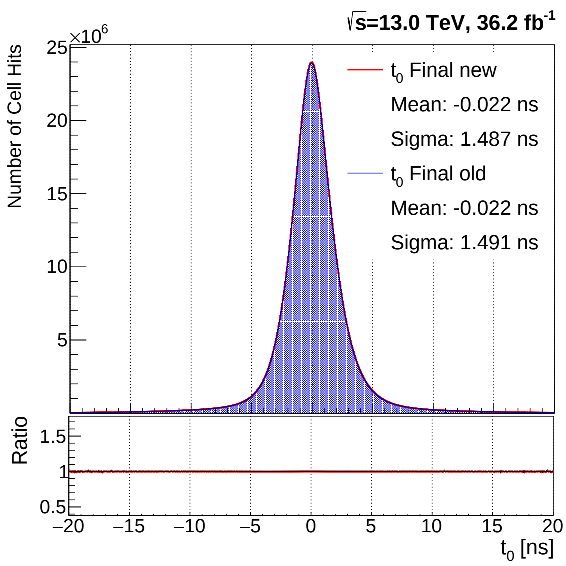

FIGURE 6.7: The t_0 distribution for all cells in the TileCal for muons in data after all calibrations using only one set of calibration parameters and using four different sets of calibration parameters. The standard deviation of the latter is slightly smaller, hinting to an improvement in the overall calibration.

6.3 Different calibration orders

The order of calibrations presented in Figure 5.1 was adapted from the previous analysis [40]. However, four different orders of the calibration steps have been tested to evaluate the difference in their overall performance. The distance correction was always done first, as it is a real correction and not a calibration of dependencies. The tested orders are:

1. Cell-wise, ϕ, energy, run-wise, η
2. Energy, run-wise, cell-wise, ϕ, η
3. η, ϕ, run-wise, cell-wise, energy
4. ϕ, cell-wise, η, energy, run-wise

The tests have been done only for 2015 and 2016 data, amounting to a total of 36.2 fb^{-1}. The calibration with the 'standard' order of steps yielded a t_0 distribution with a mean of -0.022 ns and a standard deviation of 1.451 ns (shown in Figure A.1a). The results of the calibration for the four different calibration orders are shown in Figure 6.8.

It is clearly visible, that the first two of the tested orders yielded results much worse than that achieved with the 'standard' order. This is due to the η calibration being last. That results in the earlier calibrations using a wrong estimation of the travelled time by the particle in the respective cell. Therefore the calibrations done before the η step are mis-calibrating the respective dependencies.
Furthermore, when looking at the mean of the respective t_0 distribution, for the first two tested orders the mean was significantly over-corrected. That is again due to the η calibration being the last step in the respective order. In the 'standard' calibration, the η step is responsible for shifting the mean towards the optimal value of 0 ns. In the first two tested orders however, the other calibration steps, especially the energy calibration, are shifting the mean due to the overall distribution still being shifted away from 0 ns. The η calibration as last step is then calibrating the dependency, resulting in an additional shift in the same direction, leading to the mentioned over-correction.

The third and fourth of the tested orders are both calibrating the overall t_0 distribution almost as good as the 'standard' order, with only a difference of 2 and 1 ps, respectively. The third order is even shifting the mean closer to 0 ns than the 'standard' order, but the standard deviation still is slightly worse. The origin of this effect is still unclear, but is an interesting topic for future analyses.

The best overall results, however, have been achieved with the 'standard' order of calibration steps.

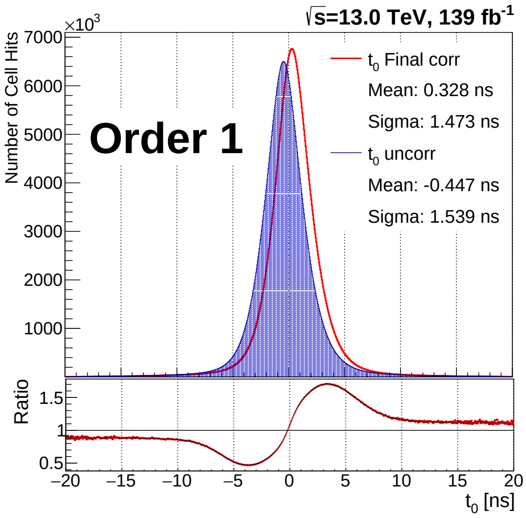

(A)

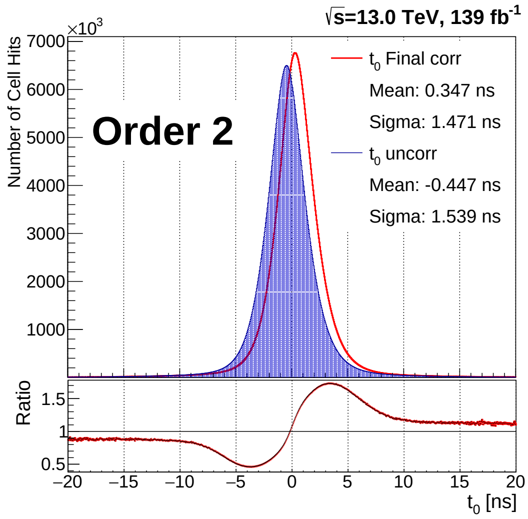

(B)

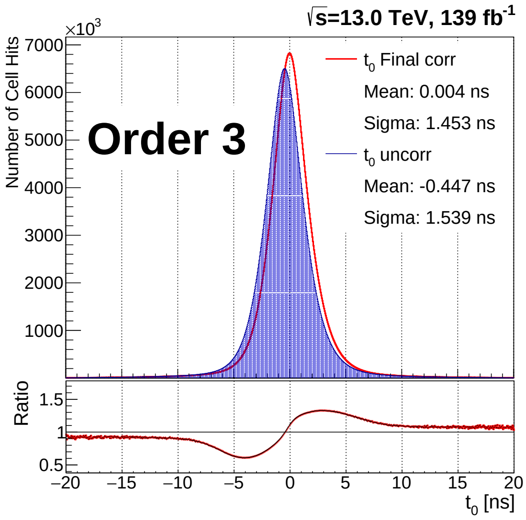

(C)

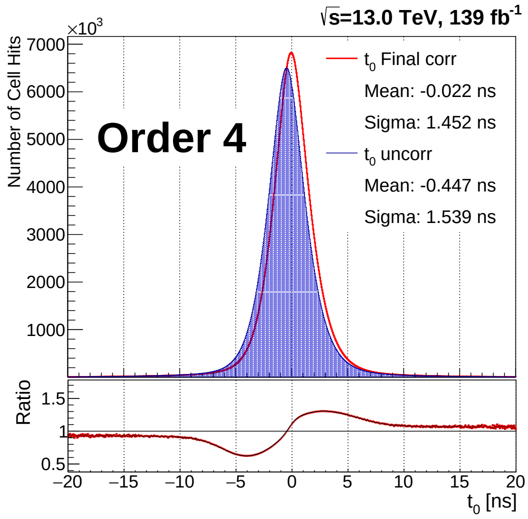

(D)

FIGURE 6.8: The t_0 distribution for all TileCal cells before and after all calibrations for muons in data. (A) shows the distribution for the first of the tested calibration orders, (B) for the second, (C) for the third and (D) for the fourth.

Chapter 7

Conclusion and Outlook

In this thesis, a calibration of the timing measurement in the ATLAS Tile calorimeter was presented. A geometrical distance correction and 5 separate calibration steps, calibrating the timing measurement from several dependencies on different variables have been applied. The distance correction and the η calibration combined are responsible for the largest part of the improvements of the timing resolution. The other calibration steps do not improve the overall resolution as much as the former steps, but are nonetheless important to ensure a stable timing measurement.
These calibration steps, excluding the cell-wise and run-wise calibrations, have also been applied to simulated events. Comparing the resulting t_0 distributions shows a clear underestimation of the uncertainty of the timing measurement in simulated events. Therefore a smearing is applied to match the actual quality of the timing measurement observed in data. To adjust the uncertainties of the β measurement, a pull correction is applied as final step.
Originating from the ToF measurement in the TileCal cells, the velocity of the particles, with respect to the speed of light, β has been calculated. Combining multiple β measurements of one particle to a combined β_{Tile} achieved an even better β resolution.

The results of this thesis have been compared to results of a previous analysis, leading to the conclusion, that the overall timing resolution has improved, but the overall β resolution is slightly worse than that achieved in the previous estimation.
Furthermore it could be observed, that the overall timing resolution as well as the overall β resolution have regressed over the four years of Run–2 data-taking. That is a discovery which brings mild concern, as a timing measurement as good as possible is crucial for an efficient search for HCLLPs using the ToF method (see Chapter 4). In regard to that effect, it could be an interesting topic to study the reasons for that regression carefully to possibly erase that decrease of the resolution.
Furthermore, lower energy thresholds have been tested, to investigate their impact on the overall β measurement. It could be observed, that the available statistics and, more important, the average number of TileCal cell hits per particle is increasing with lower energy thresholds, however the timing resolution regressed. Overall these two effects lead to a slightly worsened β resolution for lower energy thresholds, leaving the applied threshold of 500 MeV per cell hit as the most beneficial towards the β measurement.
The order of the applied calibration steps has also been tested by trying a total of five different calibration orders. The results showed, that the order also used in the previous analysis still yielded the best overall results. Nevertheless, it could be interesting to look for other possible dependencies to further improve the timing resolution. Also further work on the technicalities of the calibration, like using multiple sets of calibration parameters (see Section 6.2), could yield future improvements.

To validate the performance of the TileCal timing measurement for out-of-time hits, an investigation of muons originating from satellite–satellite collisions has been done. Unfortunately no procedure to sufficiently resolve the signals of those satellite–satellite muons could be implemented. However, with more time in a future analysis it could be interesting to investigate, how the TileCal timing measurement performs for out-of-time signals and if that specific timing performance has changed over the time span of Run–2 like the timing and β measurement have.

For the search for HCLLPs with the ATLAS detector, it is useful to combine the timing measurements of the TileCal with the timing measurement in the muon spectrometer. An analysis calibrating the timing measurement with the MS is currently in progress, so combining the conclusions of both analyses could result in further improvements.

Appendix A

Comparisons between different conditions for the calibration

A.1 Comparison with previous analysis

As explained in Chapter 5, this thesis is based on a previous analysis [26]. That preceding analysis has been done before Run-2 was completed, therefore only 2015 and 2016 data amounting to 36.1 fb^{-1} has been used. To compare the results of this thesis with the previous analysis, the calibration presented in Chapter 5 has been applied to 2015 and 2016 data only. The results of both the previous and current analyses can be found in Figure A.1. The overall effect of the previous calibration was a bit higher with a relative improvement of the timing resolution of about 6.5% compared to that of the current calibration with 5.7%. However, the uncorrected uncertainties as well as the final corrected uncertainties are improved compared to the previous analysis. That effect could origin from an overall improved reconstruction and software upgrades, but theses effects have not been studied in detail in this thesis.

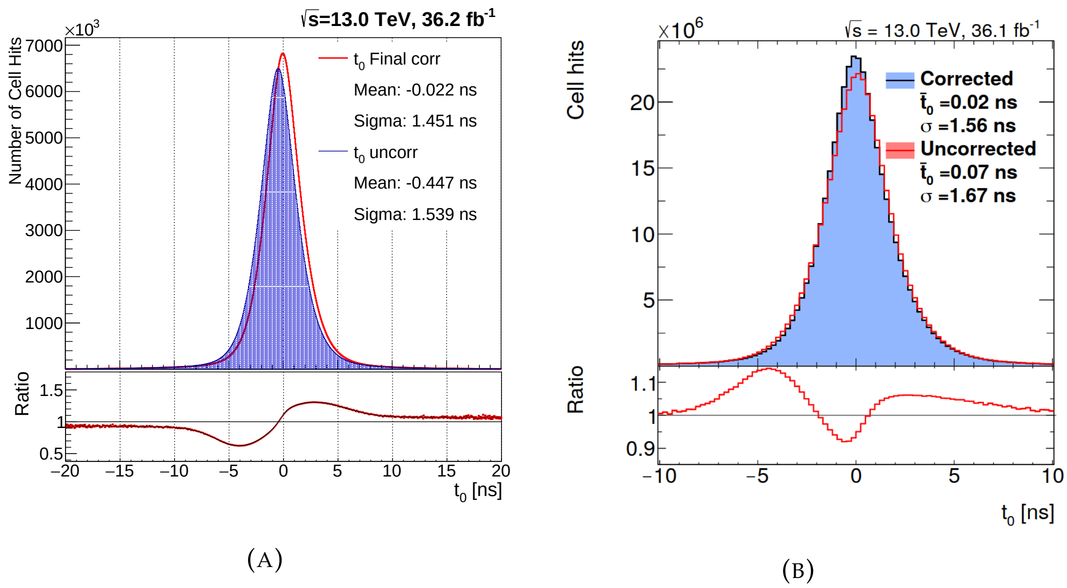

FIGURE A.1: The t_0 distribution for all TileCal cells before and after all calibrations for muons in data. (A) shows the distributions for 2015 and 2016 data achieved in this thesis, whereas (B) shows the distributions from the previous analysis [26].

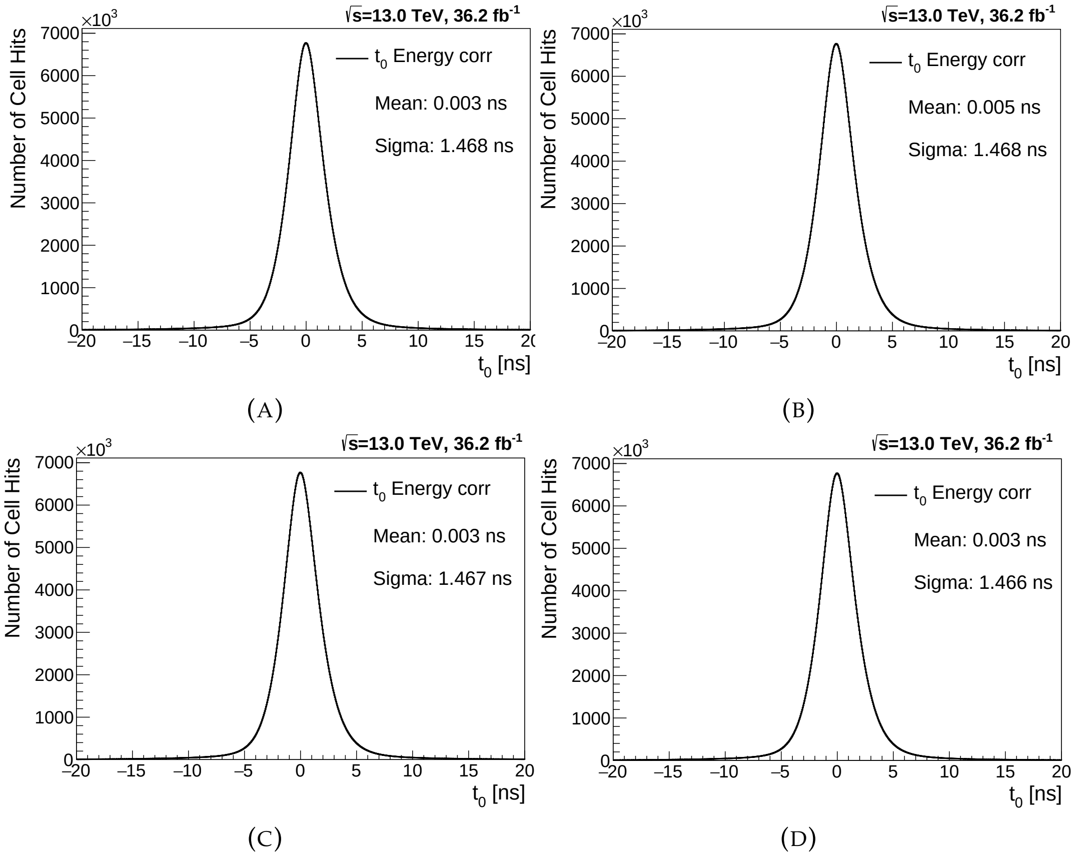

FIGURE A.2: The t_0 distribution for all TileCal cells for muons in data after the energy calibration. (A) shows the distribution for the logarithmic binning with 100 bins, (B) for the equal statistic binning with 30 bins, (C) for the equal statistic binning with 50 bins and (D) for the equal statistic binning with 100 bins. The distribution for the equal statistics binning with 100 bins shows the best uncertainty of the distributions.

A.2 Comparison between different Energy binnings

As explained in Section 5.2.4, the calibration parameters for the energy calibration have been calculated by slicing the 2D histogram showing the dependency of t_0 on the energy deposit per cell E_{Hit} into separate distributions for every single E_{Hit} bin. As mentioned, the statistics are decreasing drastically for increasing E_{Hit} values, leading to the necessity of non-constant bin sizes.
Two different binning concepts have been tested: One logarithmic binning, logarithmically increasing the bin sizes for increasing E_{Hit}, and equal statistics binnings, setting the bin sizes so that every bin includes approximately the same amount of cell hits. For the latter concept, three different bin amounts have been tested: 30 bins, 50 bins and 100 bins.

The results of the four different binnings are shown in Figure A.2. It can be seen, that the equal statistics binning with 100 bins yielded the best calibration results, therefore that binning concept has been used in this thesis. Equal statistics binnings with even more bins (200 and 300, respectively) have been investigated, but did not yield any further improvements.

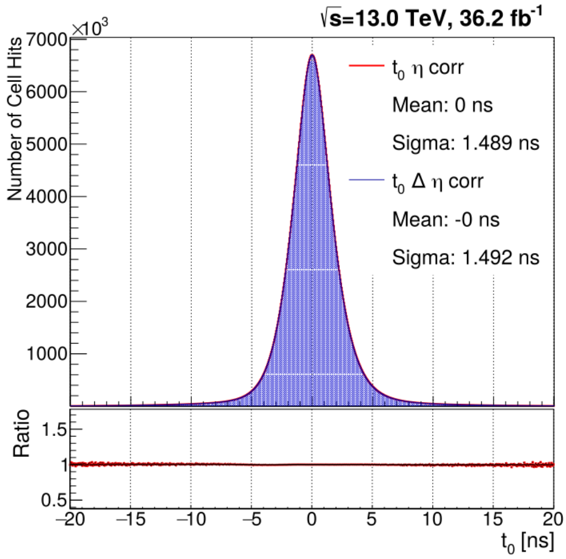

FIGURE A.3: The t_0 distribution for all cells in the TileCal for muons in data after the η-dependent calibration using $\Delta\eta$ as variable and using η as calibration variable.

A.3 Comparison between two different definitions for the η calibration

The η calibration as discussed in Section 5.2.2 has been applied to calibrate the dependency of the t_0 measurement on the variable η. This step is applied to calibrate for the mis-estimated ToF of the particle in the respective TileCal cell. Instead of using the dependency on η however, another variable could be used to calibrate for that same dependency: the difference between the η value of the particle track η_{track} and the η value of the cell centre η_{cell}:

$$\Delta\eta = \eta_{track} - \eta_{cell}. \tag{A.1}$$

The calibration with $\Delta\eta$ is done analogously to the η calibration. The comparison between the results of both calibrations can be found in Figure A.3. The calibration with the variable η yields slightly better results with the uncertainty being 1.489 ns in contrast to 1.492 ns for the $\Delta\eta$ calibration. Therefore, the η calibration in this thesis has used the variable η.

A.4 Comparison between different cell-wise calibrations

The cell-wise calibration step presented in Section 5.2.5 has calibrated the t_0 measurement in every single of the 4672 TileCal cells separately from characteristic desynchronisations. However, for the other calibration steps the ϕ-projected cells have been used, so it could be interesting to investigate, how the cell-wise calibration would act on ϕ-projected cells. Therefore this particular calibration step has been done using the ϕ-projected cells instead od the single cells. The comparison between these two different approaches can be found in Figure A.4. The uncertainty of the t_0 distribution after the cell-wise calibration using the single cells is clearly improved in contrast to that using the ϕ-projected cells. Therefore the single cell approach has been used in this thesis.

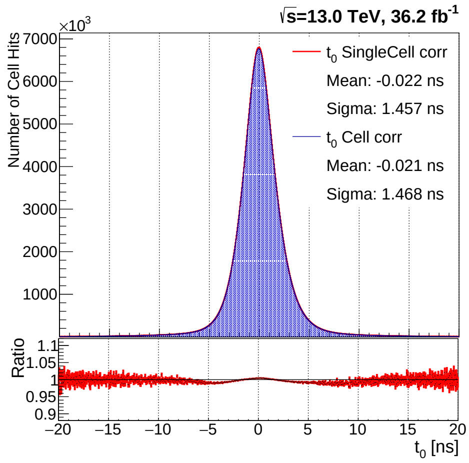

FIGURE A.4: The t_0 distribution for all cells in the TileCal for muons in data after the cell-wise calibration using ϕ-projected cells for the calibration and using each single cell for the calibration.

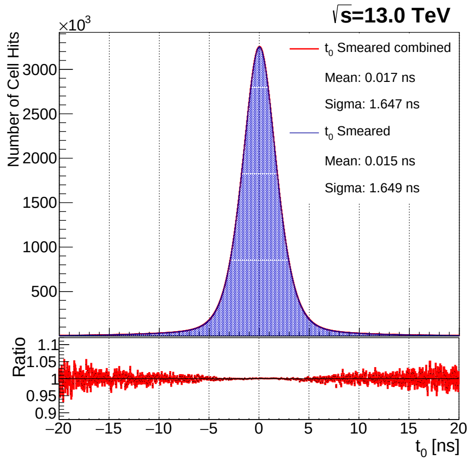

FIGURE A.5: The t_0 distribution for all cells in the TileCal for muons in simulation after the smearing using all *phi*-projected cells for the smearing and using combined cells for the smearing.

A.5 Comparison between different smearing definitions

As explained in Section 5.2.7, the smearing step was applied to muons in MC simulation. As the sample size of the simulated events was much smaller than that of muons in data, both sides of the detector have been combined to increase the available statistics in the calculation of the smearing parameters. That this procedure yields an improvement is shown Figure A.5. The uncertainty of the smeared t_0 distribution using the combined ϕ-projected cells is slightly better than that using the uncombined ϕ-projected cells.

Bibliography

[1] Isobel Falconer. "J J Thomson and the discovery of the electron". In: *Physics Education* 32.4 (1997), pp. 226–231. DOI: 10.1088/0031-9120/32/4/015. URL: https://doi.org/10.1088%2F0031-9120%2F32%2F4%2F015.

[2] David J Griffiths. *Introduction to elementary particles; 2nd rev. version*. Physics textbook. New York, NY: Wiley, 2008. URL: https://cds.cern.ch/record/111880.

[3] R Alkofer and J Greensite. "Quark confinement: the hard problem of hadron physics". In: *Journal of Physics G: Nuclear and Particle Physics* 34.7 (2007), S3–S21. ISSN: 1361-6471. DOI: 10.1088/0954-3899/34/7/s02. URL: http://dx.doi.org/10.1088/0954-3899/34/7/S02.

[4] Planck Collaboration. *Planck 2015 results. XIII. Cosmological parameters*. 2015. arXiv: 1502.01589 [astro-ph.CO].

[5] nobelprize.org. *The Nobel Prize in Physics 2004*. 2020. URL: https://www.nobelprize.org/prizes/physics/2004/popular-information/ (visited on 07/07/2020).

[6] Roger Ellman. *The Problem of Big Bang Matter vs. AntiMatter Symmetry*. 2000. arXiv: physics/0007058 [physics.gen-ph].

[7] Tarun Grover, D. N. Sheng, and Ashvin Vishwanath. "Emergent Space-Time Supersymmetry at the Boundary of a Topological Phase". In: *Science* 344.6181 (2014), pp. 280–283. ISSN: 0036-8075. DOI: 10.1126/science.1248253. eprint: https://science.sciencemag.org/content/344/6181/280.full.pdf. URL: https://science.sciencemag.org/content/344/6181/280.

[8] STEPHEN P. MARTIN. "A SUPERSYMMETRY PRIMER". In: *Advanced Series on Directions in High Energy Physics* (1998), 1–98. ISSN: 1793-1339. DOI: 10.1142/9789812839657_0001. URL: http://dx.doi.org/10.1142/9789812839657_0001.

[9] CERN. *The Large Hadron Collider*. 2020. URL: https://home.cern/science/accelerators/large-hadron-collider (visited on 07/04/2020).

[10] Vladimir Shiltsev and Frank Zimmermann. *Modern and Future Colliders*. 2020. arXiv: 2003.09084 [physics.acc-ph].

[11] N.M.A. *LHC Facts*. 2017. URL: http://www.lhc-facts.ch/ (visited on 07/04/2020).

[12] J. T. Boyd. *LHC Run-2 and Future Prospects*. 2020. arXiv: 2001.04370 [hep-ex].

[13] CERN. *ALICE*. 2020. URL: https://home.cern/science/experiments/alice (visited on 07/05/2020).

[14] CERN. *LHCb*. 2020. URL: https://home.cern/science/experiments/lhcb (visited on 07/05/2020).

[15] "Determination of the top-quark pole mass using $t\bar{t}$ + 1-jet events collected with the ATLAS experiment in 7 TeV pp collisions". In: ().

[16] G. Aad et al. "Charged-particle distributions in pp interactions at $\sqrt{s} = 8\,\text{TeV}$ measured with the ATLAS detector". In: *The European Physical Journal C* 76.7 (2016). ISSN: 1434-6052. DOI: 10.1140/epjc/s10052-016-4203-9. URL: http://dx.doi.org/10.1140/epjc/s10052-016-4203-9.

[17] G Aad. "The ATLAS Experiment at the CERN Large Hadron Collider". In: *JINST* 3 (2008). Also published by CERN Geneva in 2010, S08003. 437 p. DOI: 10.1088/1748-0221/3/08/S08003. URL: http://cds.cern.ch/record/1129811.

[18] CERN. *Inner Detector*. 2020. URL: https://atlas.cern/discover/detector/inner-detector (visited on 07/07/2020).

[19] V. A. MITSOU. "THE ATLAS TRANSITION RADIATION TRACKER". In: *Astroparticle, Particle and Space Physics, Detectors and Medical Physics Applications* (2004). DOI: 10.1142/9789812702708_0073. URL: http://dx.doi.org/10.1142/9789812702708_0073.

[20] G. Aad et al. "The ATLAS Inner Detector commissioning and calibration". In: *The European Physical Journal C* 70.3 (2010), 787–821. ISSN: 1434-6052. DOI: 10.1140/epjc/s10052-010-1366-7. URL: http://dx.doi.org/10.1140/epjc/s10052-010-1366-7.

[21] G. Aad et al. "Electron and photon energy calibration with the ATLAS detector using LHC Run 1 data". In: *The European Physical Journal C* 74.10 (2014). ISSN: 1434-6052. DOI: 10.1140/epjc/s10052-014-3071-4. URL: http://dx.doi.org/10.1140/epjc/s10052-014-3071-4.

[22] J del Peso. *Design and Performance of the ATLAS LAr Calorimeter*. Tech. rep. ATL-LARG-PROC-2011-003. Geneva: CERN, 2011. URL: https://cds.cern.ch/record/1385899.

[23] N J Buchanan and L Chen. "Design and implementation of the Front End Board for the readout of the ATLAS liquid argon calorimeters". In: *Journal of Instrumentation* 3.03 (2008), P03004–P03004. DOI: 10.1088/1748-0221/3/03/p03004. URL: https://doi.org/10.1088%2F1748-0221%2F3%2F03%2Fp03004.

[24] *ATLAS tile calorimeter: Technical Design Report*. Technical Design Report ATLAS. Geneva: CERN, 1996. URL: https://cds.cern.ch/record/331062.

[25] The ATLAS Collaboration. "The ATLAS Experiment at the CERN Large Hadron Collider". In: *Journal of Instrumentation* 3.08 (2008), S08003–S08003. DOI: 10.1088/1748-0221/3/08/s08003. URL: https://doi.org/10.1088%2F1748-0221%2F3%2F08%2Fs08003.

[26] Michael Adersberger. "Searches for Heavy Charged Long-Lived Particles with the ATLAS Detector". PhD thesis. Ludwig-Maximilians-Universität München, Nov. 2018.

[27] G. Aad et al. "Commissioning of the ATLAS Muon Spectrometer with cosmic rays". In: *The European Physical Journal C* 70.3 (2010), 875–916. ISSN: 1434-6052. DOI: 10.1140/epjc/s10052-010-1415-2. URL: http://dx.doi.org/10.1140/epjc/s10052-010-1415-2.

[28] CERN. *Muon Spectrometer*. 2020. URL: https://atlas.cern/discover/detector/muon-spectrometer (visited on 07/09/2020).

[29] E. Diehl. *Calibration and Performance of the ATLAS Muon Spectrometer*. 2011. arXiv: 1109.6933 [physics.ins-det].

[30] M. Aaboud et al. "Search for heavy charged long-lived particles in proton–proton collisions at $\sqrt{s} = 13\,\text{TeV}$ using an ionisation measurement with the ATLAS detector". In: *Physics Letters B* 788 (2019), 96–116. ISSN: 0370-2693. DOI: 10.1016/j.physletb.2018.10.055. URL: http://dx.doi.org/10.1016/j.physletb.2018.10.055.

[31] M. Fairbairn et al. "Stable Massive Particles at Colliders". In: *Phys. Rept.* 438 (2007), pp. 1–63. DOI: 10.1016/j.physrep.2006.10.002. arXiv: hep-ph/0611040.

[32] Damian C. Swift and James M. McNaney. *Approximate, analytic solutions of the Bethe equation for charged particle range*. 2009. arXiv: 0901.4145 [cond-mat.other].

[33] Michal Marcisovsky. "Operational experience of the ATLAS pixel detector". In: *Journal of Instrumentation* 6.12 (2011), pp. C12001–C12001. DOI: 10.1088/1748-0221/6/12/c12001. URL: https://doi.org/10.1088%2F1748-0221%2F6%2F12%2Fc12001.

[34] G. Aad et al. "ATLAS data quality operations and performance for 2015–2018 data-taking". In: *Journal of Instrumentation* 15.04 (2020), P04003–P04003. ISSN: 1748-0221. DOI: 10.1088/1748-0221/15/04/p04003. URL: http://dx.doi.org/10.1088/1748-0221/15/04/P04003.

[35] G. Aad et al. "Muon reconstruction performance of the ATLAS detector in proton–proton collision data at $\sqrt{s} = 13\,\text{TeV}$". In: *The European Physical Journal C* 76.5 (2016). ISSN: 1434-6052. DOI: 10.1140/epjc/s10052-016-4120-y. URL: http://dx.doi.org/10.1140/epjc/s10052-016-4120-y.

[36] Milos Dordevic. *Electroweak precision measurements in CMS*. 2017. arXiv: 1708.09409 [hep-ex].

[37] Michael Adersberger. "Studies on Velocity Measurements with theATLAS Calorimeters for the Search for HeavyLong-Lived Particles". MA thesis. Ludwig-Maximilians-Universität München, June 2015.

[38] Adam Jeff. "A Longitudinal Density Monitor for the LHC". Presented 11 Dec 2012. 2012. URL: https://cds.cern.ch/record/1513180.

[39] P. Baudrenghien et al. "The New RF control system for the CERN SPS accelerator". In: *Conf. Proc. C* 960610 (1996). Ed. by S. Myers et al., pp. 1757–1759.

[40] M. Aaboud et al. "Search for heavy charged long-lived particles in the ATLAS detector in 36.1 fb^{-1} of proton-proton collision data at $\sqrt{s} = 13\,\text{TeV}$". In: *Physical Review D* 99.9 (2019). ISSN: 2470-0029. DOI: 10.1103/physrevd.99.092007. URL: http://dx.doi.org/10.1103/PhysRevD.99.092007.

Acknowledgements

This masters thesis could not been done without the help and support of several people. Therefore, I want to thank all the people which contributed to this work in any way:

- First and foremost, I want to thank Dr. habil. Sascha Mehlhase for the supervision of this thesis and the positive attitude in his research group. His input and support greatly influenced this thesis and helped me completing this work.
- I want to thank Prof. Dr. Dorothee Schaile for the possibility to write this thesis at her chair and for the very good working environment.
- Ferdinand Krieter for countless hours of support with big and small problems, help with software questions and tips, how to improve many tasks.
- Philipp Seifermann for the very good collaboration during the whole time writing this thesis. Especially in the later parts, when the usual working environment wasn't available anymore, he was a constant support and our own little office helped me a lot finishing this thesis.
- The whole chair for elementary particle physics for the friendly environment, the joint lunches in the cafeteria and countless ping-pong breaks in the basement.
- Maximilian Kühn for the help with the Lateχ template and lots of motivation in the latter parts of this thesis.

Declaration of Authorship

Hiermit erkläre ich, die vorliegende Arbeit selbstständig verfasst zu haben und keine anderen als die in der Arbeit angegebenen Quellen und Hilfsmittel benutzt zu haben.

München,

Unterschrift:
